
Research Article: New Research | Development

Carrier of Wingless (Cow) Regulation of *Drosophila* Neuromuscular Junction Development

<https://doi.org/10.1523/ENEURO.0285-19.2020>

Cite as: eNeuro 2020; 10.1523/ENEURO.0285-19.2020

Received: 18 July 2019

Revised: 9 January 2020

Accepted: 27 January 2020

This Early Release article has been peer-reviewed and accepted, but has not been through the composition and copyediting processes. The final version may differ slightly in style or formatting and will contain links to any extended data.

Alerts: Sign up at www.eneuro.org/alerts to receive customized email alerts when the fully formatted version of this article is published.

Copyright © 2020 Kopke et al.

This is an open-access article distributed under the terms of the Creative Commons Attribution 4.0 International license, which permits unrestricted use, distribution and reproduction in any medium provided that the original work is properly attributed.

1 **Carrier of Wingless (Cow) Regulation of *Drosophila* Neuromuscular Junction**

2 **Development**

3

4 Abbreviated Title: Carrier of Wingless Regulates Synapse Development

5

6 Author Names and Affiliations:

7 Danielle L. Kopke¹, Shannon N. Leahy¹, Dominic J. Vita¹, Sofia C. Lima¹,

8 Zachary L. Newman² and Kendal Broadie¹

9

10 ¹Department of Biological Sciences, Kennedy Center for Research on Human

11 Development, Vanderbilt University, Nashville, TN 37235, USA

12 ²Department of Molecular and Cell Biology, University of California, Berkeley, Berkeley,

13 CA 94720, USA

14

15 Author Contributions:

16 D.L.K., S.C.L. and K.B. designed the research program; D.L.K., S.N.L., S.C.L. and

17 D.J.V. performed the research; D.L.K., S.N.L., S.C.L., Z.L.N. and D.J.V. analyzed data.

18 D.L.K. and K.B. wrote the manuscript, and all authors edited the manuscript.

19 Correspondence: kendal.broadie@vanderbilt.edu

20

21 Conflict of Interest: The authors report no conflict of interest.

22 Funding Sources: This work was supported by National Institutes of Health grant

23 MH096832 to K.B. and F31MH111144 to D.L.K.

24 **Abstract**

25 The first Wnt signaling ligand discovered, *Drosophila* Wingless (Wg; Wnt1 in mammals),
26 plays critical roles in neuromuscular junction (NMJ) development, regulating synaptic
27 architecture and function. Heparan sulfate proteoglycans (HSPGs), consisting of a core
28 protein with heparan sulfate (HS) glycosaminoglycan (GAG) chains, bind to Wg ligands
29 to control both extracellular distribution and intercellular signaling function. *Drosophila*
30 HSPGs previously shown to regulate Wg *trans*-synaptic signaling at the NMJ include
31 the glypican Dally-like Protein (Dlp) and perlecan Terribly Reduced Optic Lobes (Trol).
32 Here, we investigate synaptogenic functions of the most recently described *Drosophila*
33 HSPG, secreted Carrier of Wingless (Cow), which directly binds Wg in the extracellular
34 space. At the glutamatergic NMJ, we find that Cow secreted from the presynaptic motor
35 neuron acts to limit synaptic architecture and neurotransmission strength. In *cow* null
36 mutants, we find increased synaptic bouton number and elevated excitatory current
37 amplitudes, phenocopying presynaptic Wg overexpression. We show *cow* null mutants
38 exhibit an increased number of glutamatergic synapses and increased synaptic vesicle
39 (SV) fusion frequency based both on GCaMP imaging and electrophysiology recording.
40 We find that membrane-tethered Wg prevents *cow* null defects in NMJ development,
41 indicating that Cow mediates secreted Wg signaling. It was shown previously that the
42 secreted Wg deacylase Notum restricts Wg signaling at the NMJ, and we show here
43 that Cow and Notum work through the same pathway to limit synaptic development.
44 We conclude Cow acts cooperatively with Notum to coordinate neuromuscular synapse
45 structural and functional differentiation via negative regulation of Wg *trans*-synaptic
46 signaling within the extracellular synaptomatrix.

47 **Significance Statement**

48 Wnt intercellular signaling is disrupted in numerous devastating neurological disorders,
49 including Alzheimer's disease. Therefore, an understanding of Wnt signaling regulation
50 is important for the design and implementation of targeted treatments. As a disease
51 model, the *Drosophila* glutamatergic NMJ system is large, accessible and genetically
52 malleable, and thus well suited for discovering the molecular and cellular mechanisms
53 of Wnt signaling regulation. Extracellular HSPGs are important players as regulators of
54 Wnt intercellular signaling. Here, we show secreted HSPG Carrier of Wingless (Cow),
55 which directly binds to the founding Wnt-1 ligand, regulates NMJ structure and function.
56 The mammalian homolog of Cow, Testican-2, is highly expressed in the brain. Studying
57 this HSPG in *Drosophila* should inform mechanisms of Wnt regulation in human brain.

58

59 **Introduction**

60 The developing nervous system requires the coordinated action of many signaling
61 molecules to ensure proper synapse formation and function. One key class of signals is
62 the Wnt ligands. The first discovered Wnt, *Drosophila* Wingless (Wg), is secreted from
63 presynaptic neurons (Packard et al., 2002) and glia (Kerr et al., 2014) at the developing
64 glutamatergic neuromuscular junction (NMJ) to bind to the Frizzled-2 (Fz2) receptor
65 (Bhanot et al., 1996) in both anterograde and autocrine signaling. In the postsynaptic
66 muscle, Wg binding to Fz2 activates the non-canonical Frizzled Nuclear Import (FNI)
67 pathway, which leads to Fz2 endocytosis and cleavage of the Fz2 C-terminus (Mathew
68 et al., 2005). The Fz2-C fragment is trafficked to the nucleus to control translation of
69 synaptic mRNAs and glutamate receptors (GluRs; Speese et al., 2012). In presynaptic

70 neurons, Wg binding to Fz2 activates a divergent canonical pathway inhibiting glycogen
71 synthase kinase 3 β (GSK3 β) homolog Shaggy (Sgg) to control microtubule cytoskeletal
72 dynamics via the microtubule-associated protein 1B (MAP1B) homolog Futsch (Miech et
73 al., 2008), resulting in synaptic bouton growth (Franco et al., 2004; Ataman et al., 2008).
74 The Wg signaling ligand must be tightly regulated in the synaptic extracellular space
75 (synaptomatrix) to ensure proper NMJ development.

76 One critical category of proteins regulating Wg ligand in the synaptomatrix is
77 heparan sulfate proteoglycans (HSPGs; Kamimura and Maeda, 2017). HSPGs consist
78 of a core protein to which heparan sulfate (HS) glycosaminoglycan (GAG) chains are
79 covalently attached. HS GAG chains are composed of repeating disaccharide subunits
80 expressing variable sulfation patterns (the “sulfation code”; Masu, 2016). These GAG
81 chains bind secreted extracellular ligands to regulate intercellular signaling. There are 3
82 HSPG families: transmembrane, GPI-anchored and secreted. The *Drosophila* genome
83 encodes only 5 HSPGs, with 3 known to affect NMJ development; transmembrane
84 Syndecan (Johnson et al., 2006), GPI-anchored Dally-like Protein (Dlp; Johnson et al.,
85 2006; Dani et al., 2012), and secreted Perlecan (Kamimura et al., 2013). A second
86 secreted HSPG recently characterized in *Drosophila* was named Carrier of Wingless
87 (Cow; Chang and Sun, 2014). In the developing wing disc, Cow directly binds secreted
88 Wg and promotes its extracellular transport in an HS-dependent manner. Cow shows a
89 biphasic effect on Wg target genes. Removing Cow results in a Wg overexpression
90 phenotype for short-range targets, and a loss-of-function phenotype for long-range
91 targets (Chang and Sun, 2014).

92 The mammalian homolog of Cow, Testican-2, is highly expressed within the
93 developing mouse brain (Vannahme et al., 1999), and inhibits neurite extension in
94 cultured neurons (Schnepp et al., 2005), although the mechanism of action is not
95 known. We therefore set out to characterize Cow functions at the developing *Drosophila*
96 NMJ. We use the larval NMJ model because it is large, accessible and particularly well
97 characterized for HSPG-dependent Wg *trans*-synaptic signaling (Sears and Broadie,
98 2018). Each NMJ terminal consists of a relatively stereotypical innervation pattern, with
99 consistent axonal branching and synaptic bouton formation (Menon et al., 2013).
100 Boutons are the functional unit of the NMJ, containing presynaptic components required
101 for neurotransmission including glutamate-containing synaptic vesicle (SV) pools and
102 specialized active zone (AZ) sites for SV fusion. AZs contain Bruchpilot (Brp) scaffolds,
103 which both cluster Ca²⁺ channels (Kittel et al., 2006) and tether SVs (Hallermann et al.,
104 2010). AZs are directly apposed to glutamate receptor (GluR) clusters in the
105 postsynaptic muscle membrane (Schuster et al., 1991). This spatially precise
106 juxtaposition is critical for high-speed and efficient synaptic communication between
107 neuron and muscle.

108 In this study, we sought to test Cow functions at the NMJ, with the hypothesis
109 that Cow should facilitate extracellular Wg transport across the synapse. Structurally,
110 *cow* null mutants display overelaborated NMJs with more boutons and more synapses,
111 phenocopying Wg overexpression. This phenotype is replicated with targeted neuronal
112 Cow knockdown, but not muscle Cow knockdown, consistent with Cow secretion from
113 the presynaptic terminal. Functionally, *cow* null mutants display increased synaptic
114 transmission strength. Both electrophysiology recording and postsynaptically targeted

115 GCaMP imaging show increased SV fusion, indicating elevated presynaptic function.
116 Replacing native Wg with a membrane-tethered Wg blocks secretion (Alexandre et al.,
117 2014). Tethered Wg has little effect on NMJ development, but when combined with the
118 *cow* null suppresses the synaptic bouton increase, indicating that Cow mediates only
119 secreted Wg signaling. It was recently shown that Notum, a secreted Wg deacylase,
120 also restricts Wg signaling at the NMJ (Kopke et al., 2017). We show here that
121 combining null *cow* and *notum* heterozygous mutants causes a synergistic increase in
122 NMJ development, indicating nonallelic noncomplementation. Moreover, combining null
123 *cow* and *notum* homozygous mutants did not cause an increase in NMJ development
124 compared to the single nulls, indicating an interaction within the same pathway. We
125 conclude that Cow functions via negative regulation of Wg *trans*-synaptic signaling.

126

127 **Materials & Methods**

128 ***Drosophila* genetics**

129 All *Drosophila* stocks were reared on standard cornmeal/agar/molasses food at 25°C in
130 a 12-hour light/dark cycling incubator. Mixed sexes were used for all experiments
131 except the SynapGCaMP imaging (females only). The genetic background control
132 was *w*¹¹¹⁸. The *cow*^{5Δ} mutant, *UAS-cow-miRNA-1* (referred to as *UAS-cow-RNAi*) and
133 *UAS-SP-eGFP-cow* (referred to as *UAS-Cow::eGFP*) lines (Chang and Sun, 2014) were
134 obtained from Yi Henry Sun (Institute of Molecular Biology, Academia Sinica, Taipei,
135 Taiwan). The *cow*^{GDP} #03259 (*y*[1] *w*[*]; *Mi*{*y*+*mDint2*}=MIC)Cow[MI03259]/TM3, *Sb*[1]
136 *Ser*[1]) and *cow*^{GDP} #12802 (*y*[1] *w*[*]; *Mi*{*y*+*mDint2*}=MIC)Cow[MI12802]) mutants, and
137 the *cow* Df #6193 (*w*[1118]; Df(3R)Exel6193, P{*w*+*mC*}=XP-U)Exel6193/TM6B, *Tb*[1])

138 and *cow* Df #619 (w[1118]; Df(3R)BSC619/TM6C, cu[1] Sb[1]) deficiencies were all
139 obtained from the Bloomington *Drosophila* Stock Center (stock numbers 40757, 58669,
140 7672 and 25694, respectively; Indiana University, Bloomington, IN, USA). *Cow-Gal4*
141 was obtained from the Vienna Tile (VT) collection of the Vienna *Drosophila* Resource
142 Center (VT046086). Neuronal *vesicular glutamate transporter (vglut)-Gal4* and muscle-
143 specific *24B-Gal4* driver lines were obtained from the Bloomington *Drosophila* Stock
144 Center. The *MHC-CD8-GCaMP6f-Sh Ca²⁺* reporter (SynapGCaMP6f; Newman et al.,
145 2017) was obtained from Ehud Isacoff (University of California, Berkeley, CA, USA).
146 Control *wg{KO; FRT Wg FRT QF; pax-Cherry}* and membrane-tethered *wg{KO; FRT*
147 *NRT-Wg FRT QF; pax-Cherry}* (Alexandre et al., 2014) were obtained with permission
148 from Andrea Page-McCaw (Department of Cell and Developmental Biology, Vanderbilt
149 University, TN, USA). Null *notum^{KO} (4)(w+)* (Kakugawa et al., 2015) was obtained from
150 Jean-Paul Vincent (Francis Crick Institute, London, UK).

151

152 **PCR/RT-PCR studies**

153 Staged *Drosophila* eggs were dechorionated using bleach for 30 secs, washed with
154 dH₂O 3X, and embryos genotyped by GFP marker with an epifluorescent microscope.
155 5 embryos per genotype were homogenized in 10µl Gloor and Engels DNA extraction
156 buffer (10 mM Tris HCL pH 8.2, 1 mM EDTA pH 8.0, 25 mM NaCl and 200 µg/mL
157 Proteinase K) with a glass rod in an Eppendorf tube, and the homogenate incubated at
158 37°C for 30 mins, and then 95°C for 2 mins. For each PCR reaction, ~10ng of DNA was
159 used with the following primers: forward 5'-GCAACATTCTGGCTTCGTGTCATGC-3'
160 and reverse 5'-CTCTCGACTTGCAAATAGCAGACGATGATC-3' for the *cow* gene

161 (product size 1927); forward 5'-GTGGAAAAGCGGTTGAAATAGGG-3' and reverse 5'-
162 GTCCACATCCACAAAGATGCC-3' for the *dfmr1* gene control (product size 3850). For
163 the RT-PCR studies, 1 embryo per genotype was used with The RNeasy Micro Kit
164 (Qiagen, 74004) to extract RNA. The OneStep RT-PCR Kit (Qiagen, 210212) was used.
165 For each reaction, ~7ng of RNA was used with the following primers: forward 5'-
166 AGAACAGCAACTTGAATGCCTATC-3' and reverse 5'-CGAAGCATCTGCACCATTCC-
167 3' for the *cow* gene (product size 348); forward 5'-TAAACTGCGAGAGGTTTTCC-3' and
168 reverse 5'- ATTCGATGAGTGACGCTG-3' for the *dmgalectin* gene control (product
169 size 321). Products were loaded on a 0.8% agarose gel in TAE buffer with purple gel
170 loading dye (NEB, B7025S) and SYBR safe DNA gel stain (ThermoFisher, S33102),
171 and run at 100V for 30 mins.

172

173 **Cow antibodies**

174 We used a well-characterized, published anti-Cow antibody (Chang and Sun, 2014).
175 New rabbit anti-Cow antibodies were also made by ABclonal (Woburn, MA) against
176 amino acids 36-236. Three antiserums were recovered and affinity purified (29, 30, 31).
177 Cow antibody 31 was pre-absorbed against *cow* nulls (*cow^{GDP}*) for imaging studies.
178 Cow antibody 31 was used for Figures 1, 2 and 4.

179

180 **Western blotting**

181 Staged *Drosophila* eggs (18-24 hour post-fertilization (hpf) for maximum expression;
182 www.fruitfly.org) were dechorionated using bleach for 30 secs, washed with dH₂O 3X,
183 and embryos genotyped by GFP marker with an epifluorescent microscope. 25 embryos

184 were placed into an Eppendorf tube with 24 μ l RIPA buffer (150 mM sodium chloride, 1%
185 Triton X-100, 0.5% sodium deoxycholate, 0.1% sodium dodecyl sulfate, 50 mM Tris)
186 and protease inhibitor cocktail (Sigma, P8340), then immediately snap-frozen in a dry
187 ice ethanol bath. Samples were sonicated (Branson Sonifier 250, settings: 90% duty,
188 output 2) for 20 secs, vortexed (Standard Mini Vortexer, VMR Scientific Products, speed
189 4) for 5 secs, and then centrifuged at 14000 RPM for 10 mins. The supernatant was
190 then transferred to new tubes with 1X NuPage LDS buffer (Invitrogen, NP007) and 5%
191 2-mercaptoethanol (Sigma, M7154), then vortexed as above. Samples were incubated
192 at RT for 20 mins, heated at 100°C for 10 mins, then centrifuged as above. Equal
193 volumes of lysate were loaded into precast NuPage 4-12% Bis-Tris gels (Invitrogen,
194 NP0336) with NuPage running buffer (Life Technologies, NP002) and NuPage
195 antioxidant (Invitrogen, NP0005). Electrophoresis was done at 150 V for 2 hrs. Protein
196 was then transferred overnight at 4°C with constant 30 mA current to nitrocellulose
197 membranes (PROTRAN, NBA085C001EA) in the NuPage transfer buffer (Life
198 Technologies, NP0006-1) supplemented with 20% methanol (Honeywell, AH230-4).
199 Following transfer, membranes were rinsed with dH₂O, air dried at RT for 1 hr, and then
200 blocked with 2% non-fat powdered milk in TBS-T (0.1% Tween-20, 150 mM sodium
201 chloride, 5mM potassium chloride, 25 mM Tris, pH 7.6) at RT for 1 hr with rotation.
202 Primary antibodies were incubated overnight in 2% milk in TBST. Membranes were then
203 washed in TBST (5x6 mins), followed by incubation in secondary antibody at RT in 2%
204 milk in TBST for 1 hr with rotation, and washed again as before. Imaging was performed
205 on a LI-COR Odyssey Imager with analysis on Image Studio Lite (LI-COR Biosciences).
206 Total protein was assessed via the REVERT total protein stain (LI-COR, 926-11011).

207 Primary antibodies: rabbit anti-Cow (this study, Ab 31) and goat anti-GFP (Abcam,
208 ab6662), both at 1:1,000. Secondary antibodies: IRDye 680 donkey anti-rabbit (LI-COR,
209 926-68073) and IRDye 800 donkey anti-goat (LI-COR, 926-32214), both at 1:10,000.

210

211 **Confocal imaging**

212 Wandering third instars were dissected in physiological solution containing (in mM): 128
213 NaCl, 2 KCl, 0.2 CaCl₂, 4 MgCl₂, 70 sucrose, 5 HEPES {2-[4-(2-hydroxyethyl)piperazin-
214 1-yl]ethanesulfonic acid} at pH 7.2. The samples were fixed with 4% paraformaldehyde
215 (EMS; 15714) diluted in PBS (Corning; 46-013-CM). For intracellular labeling, samples
216 were permeabilized with 0.2% Triton X-100 (Fisher Scientific; BP151-100) 3X for 10
217 mins each). Embryos were bleached for de-chorionation, fixed with heptane and
218 paraformaldehyde, and de-vitellinized with methanol. Primary antibodies: mouse anti-
219 DLG (4F3; 1:250), mouse anti-Wg (4D4; 1:1) and mouse anti-Brp (nc82; 1:200), all from
220 the Developmental Studies Hybridoma Bank (DSHB); Alexa Fluor 488-conjugated goat
221 anti-HRP (123-545-021; 1:250), Cy3-conjugated goat anti-HRP (123-165-021; 1:250),
222 and Alexa Fluor 647-conjugated goat anti-HRP (123-605-021; 1:250), all from Jackson
223 ImmunoResearch; rabbit anti-GluRIIC (Marrus et al., 2004; 1:5,000) and rabbit anti-GFP
224 (abcam, ab290; 1:1,500). Preparations were incubated with primary antibodies
225 overnight at 4°C and secondary antibodies at RT for 2 hrs, washed 3X for 10 mins each,
226 and then mounted in Fluoromount-G (EMS, 17984-25) onto 25x75x1mm slides (Fisher
227 Scientific, 12-544-2) with a 22x22-1 coverslip (Fisher Scientific, 12-542-B) and sealed
228 with clear nail polish (Sally Hansen). Imaging was performed on a Zeiss LSM 510
229 META laser-scanning confocal microscope, with images projected in Zen (Zeiss) and

230 analyzed using ImageJ (NIH). NMJ intensity measurements were made with HRP signal
231 delineated Z-stack areas of maximum projection using ImageJ threshold and wand-
232 tracing tools.

233

234 **TEVC electrophysiology**

235 Wandering third instars were dissected longitudinally along the dorsal midline, internal
236 organs removed, and body walls glued down (Vetbond, 3M). Peripheral motor nerves
237 were cut at the base of the ventral nerve cord (VNC). Dissections and two-electrode
238 voltage-clamp (TEVC) recordings were both carried out at 18°C in physiological saline
239 (in mM): 128 NaCl, 2 KCl, 4 MgCl₂, 1.5 CaCl₂, 70 sucrose and 5 HEPES; pH 7.2.
240 Preparations were imaged employing a Zeiss Axioskop microscope with a Zeiss 40X
241 water-immersion objective. Muscle 6 in abdominal segments 3-4 was impaled with two
242 intracellular electrodes (1-mm outer diameter borosilicate capillaries; World Precision
243 Instruments, 1B100F-4) of ~15 MΩ resistance filled with 3 M KCl. The muscles were
244 clamped at -60 mV using an Axoclamp-2B amplifier (Axon Instruments). Spontaneous
245 mEJC recordings were made in continuous 2 min sessions and low-pass filtered. For
246 EJC records, the motor nerve was stimulated with a fire-polished suction electrode
247 using 0.5 ms suprathreshold voltage stimuli at 0.2 Hz from a Grass S88 stimulator.
248 Nerve stimulation-evoked EJC recordings were filtered at 2 kHz. To quantify EJC
249 amplitude, 10 consecutive traces were averaged and the average peak value recorded.
250 Clampex 9.0 was used for data acquisition, and Clampfit 9 was used for data analysis
251 (Axon Instruments).

252

253 **SynapGCaMP imaging**

254 For SynapGCaMP quantal imaging experiments, wandering third instars were dissected
255 and type 1b NMJs imaged in physiological saline (in mM): 70 NaCl, 5 KCl, 1.5 CaCl₂, 25
256 MgCl₂, 10 NaHCO₃, 5 trehalose, 115 sucrose, 5 HEPES; pH 7.2. Fluorescence images
257 were acquired with a Vivo Spinning Disk Confocal microscope (3i Intelligent Imaging
258 Innovations, Denver, CO), with a 63X 1.0NA water immersion objective (Zeiss),
259 LaserStack 488nm (50 mW) laser, Yokogawa CSU-X1 A1 spinning disk (Tokyo, Japan),
260 and EMCCD camera (Photometrics Evolve, Tucson, AZ). Image capture and analysis
261 was performed as reported previously (Newman et al., 2017). Briefly, spontaneous
262 events were imaged at 20 Hz (50 ms exposures; streaming capture mode) for 30 secs.
263 Movies were then filtered, registered, and bleach-corrected prior to ΔF conversion.
264 Using the Delta ΔF data, a XYT local maxima algorithm was applied to the thresholded
265 ΔF data to identify where and when quantal release events occur (Newman et al.,
266 2017). Quantal coordinates were used to calculate $\Delta F/F$ amplitudes and frequencies
267 (normalized to the baseline SynapGCaMP6f 2D area).

268

269 **Structured illumination microscopy**

270 Dissected wandering third instar preparations were imaged using a Nikon N-SIM in 3D
271 SIM mode, configured with a 100x EX V-R diffraction grating, automated TiE inverted
272 fluorescence microscope stand, 100x SR Apo 1.49 NA objective, Andor DU-897 EM-
273 CCD, and 488/561nm lasers. Image acquisition was managed through NIS-Elements
274 (Nikon Instruments, Inc.), and stacks were acquired with a 0.12 μ m step size. Stack
275 reconstruction of the raw data was used prior to rendering and analysis. To acquire

276 larger fields-of-view and capture whole NMJs, SIM images were stitched together using
277 the automated tiling method within NIS-Elements software.

278

279 **LSM image analysis**

280 We used Imaris Version 9.3.0 to quantify LSM images using the “surfaces” function to
281 identify the number and volume of Brp punctae:

- 282 1. Open image file and click “add new surfaces” to start the wizard.
- 283 2. Algorithm settings click “segment only a region of interest”.
- 284 3. Select region of interest (ROI) in X, Y and Z.
- 285 4. Select “source channel” and thresholding conditions.
- 286 5. Adjust threshold until all spots are selected.
- 287 6. Enable “split touching objects” with seed points diameter (0.4 μm).
- 288 7. Use “quality filter” to adjust selections with minimal background.
- 289 8. Click “finish” to execute all creation steps and exit the wizard.
- 290 9. Click “edit” tab and delete extraneous spots by hand.
- 291 10. Click “statistics” tab and export values to Microsoft Excel.

292

293 **SIM image analysis**

294 We used Imaris Version 9.3.0 to quantify SIM images using the “spots” function to
295 identify the number of Brp punctae and GluR clusters:

- 296 1. Open image file and click “add new spots” to start the wizard.
- 297 2. Algorithm settings click “segment only a region of interest” with “different spot
298 sizes (region growing)”.

- 299 3. Select region of Interest (ROI) in X, Y and Z.
300 4. Select “source channel” and click “background subtraction”.
301 5. Classify spots with a “quality” filter type and adjust by eye.
302 6. Spot regions click “local contrast”.
303 7. Region threshold with diameter from “region volume”.
304 8. Click “finish” to execute all creation steps and exit the wizard.
305 9. Click “edit” tab and delete extraneous spots by hand.
306 10. Click “statistics” tab and export values to Microsoft Excel.

307

308 **Statistical analyses**

309 All statistical measurements were performed within GraphPad Prism (Version 7.04 for
310 Windows). The D’Agostino-Pearson K-squared normality test was done on all datasets
311 to check for normality. For comparisons of 2 genotypes, a t-test (normally distributed) or
312 Mann-Whitney test (not normally distributed) was done. For all other comparisons of >2
313 genotypes, an ordinary one-way ANOVA (normally distributed) or Kruskal-Wallis test
314 (not normally distributed) was done. All graphs were made in Prism and the data are
315 represented in scatter plots with the mean \pm standard error of the mean (SEM).

316

317 **Results**

318 **Carrier of Wingless (Cow) genetic locus, mutants and expression profiles**

319 The *cow* gene encodes 3 transcripts (*cow*-RC, -RD, -RE), with *cow*-RD containing
320 a long 3'-UTR (Fig. 1A). We acquired a reported *cow* null mutant (*cow*^{5A}; Chang and
321 Sun, 2014), two mutations from the Gene Disruption Project (*cow*^{GDP} 03259 and 12802;

322 Bellen et al., 2004; Nagarkar-Jaiswal et al., 2015) and two *cow* deficiencies from the
323 Bloomington *Drosophila* Stock Center (Df[619] and Df[6193]). The *cow*^{5Δ} mutant has a
324 9,119 bp deletion starting in the 3' UTR that does not remove *cow* coding sequence, but
325 published as a well-characterized protein null (Chang and Sun, 2014). The *cow*^{GDP} lines
326 are minos mediated integration cassette (Mi{MIC}) insertions; 03259 in *cow* intron 1,
327 and 12802 in *cow* intron 4. Df[619] completely removes *cow* and 31 other genes, while
328 *cow* Df[6193] removes *cow* and 41 other genes. PCR tests were done using primers in
329 the *cow*^{5Δ} deletion region (Fig. 1A). As expected, there are no PCR products from *cow*^{5Δ}
330 or either *cow* Df (Fig.1B). Next, RT-PCR tests were done using primers spanning an
331 exon-exon junction to ensure mRNA amplification (Fig. 1A). The RNA extraction was
332 confirmed using primers for a control gene (*dfmr1*; Fig. 1C). The *cow* transcript in the
333 genetic background control *w*¹¹¹⁸ is present at similar levels in the *cow*^{5Δ} line (Fig. 1D).
334 There is no detectable *cow* transcript in either of the *cow* Dfs, or in one of the *cow*^{gdp}
335 lines (03259), and only a very faint product in the other *cow*^{gdp} line (12802; Fig. 1D).
336 Thus, *cow*^{gdp} 03259 is an RNA null allele.

337 The published *cow*^{5Δ} mutation has been reported to have similar transcript levels
338 to wildtype, but to have no detectable Cow protein expression (Chang and Sun, 2014).
339 We therefore next examined protein levels via Western blotting using the published, well
340 characterized Cow antibody (Chang and Sun, 2014), as well as 3 new antibodies made
341 for this study (see Methods). Cow protein has a predicted molecular weight of ~75 kDa
342 (without HS chains) and ~100 kDa (with HS chains). The 2 Cow protein bands are
343 clearly present in the *w*¹¹¹⁸ controls and absent in both *cow* deficiency lines (Fig. 1E).
344 Cow protein is also undetectable in the *cow*^{gdp} lines, even at heightened levels of protein

345 loading (Fig. 1E). In stark contrast to previously published work (Chang and Sun, 2014),
346 both Cow protein bands are present at normal levels in *cow^{5Δ}* mutants (Fig. 1E, arrows).
347 In our studies, *cow^{5Δ}* mutants typically die as early stage larvae, and the few escapers
348 can be raised to the third instar only with constant care. In contrast, both *cow^{gdp}* protein
349 nulls are fully adult viable, both as homozygotes and as heterozygotes over Df[619].
350 Thus, our evidence indicates *cow^{5Δ}* does not affect Cow expression, but has a second
351 site larval lethal mutation. Further, the Cow protein is not required for full adult viability.
352 For the remainder of experiments, *cow^{gdp}* 03259 and *cow* Df[619] were used, as both
353 show complete removal of Cow RNA and protein.

354 To assess Cow protein expression in controls and null mutants, we performed
355 anti-Cow labeling and Cow-Gal4 to drive UAS-Cow::eGFP (Fig. 2). In control embryos,
356 Cow is widely expressed, including localization in the ventral nerve cord (VNC; Fig. 2A).
357 In *cow* null mutants (*cow^{GDP}/cow^{GDP}*), antibody labeling is undetectable (Fig. 2A, right).
358 Since Cow has a signal peptide, and has been previously established to be secreted
359 (Chang and Sun, 2014), we tested Cow expression at the NMJ using antibody labeling
360 with non-permeabilizing conditions. In the *w¹¹¹⁸* control wandering third instar NMJ, Cow
361 appears secreted from a dynamic subset of type 1b synaptic boutons (Fig. 2B, arrows).
362 Cow is also present in a punctate pattern along the peripheral nerve bundle
363 (arrowhead). In *cow* nulls, neuronal and synaptic antibody labeling is lost (Fig. 2B,
364 right). Within NMJ synaptic boutons co-labeled for both Cow and Wingless (Wg)
365 antibody, the two secreted proteins have overlapping expression patterns, colocalizing
366 in the extracellular synaptomatrix surrounding the same boutons (Fig. 2C). Using Cow-
367 Gal4 to drive a UAS-Cow::eGFP, GFP is present throughout the wandering third instar

368 wing imaginal disc, including punctae surrounding the wing pouch (Fig. 2D, left).
369 Cow::eGFP is also present at the NMJ, in punctae within and surrounding the synaptic
370 boutons within a single confocal slice (Fig. 2D, right). Overall, Cow is expressed in both
371 neuronal and non-neuronal tissue in embryos, larvae and imaginal discs, and co-
372 localizes with Wg in the NMJ.

373

374 **Presynaptic Cow restricts NMJ growth and synaptic bouton formation**

375 Wg *trans*-synaptic signaling regulates NMJ growth and synaptic bouton formation
376 (Packard et al., 2002), thus we hypothesized that if Cow regulates Wg at the NMJ, Cow
377 loss should affect the NMJ architecture. Each NMJ terminal consists of a relatively
378 stereotypical muscle innervation pattern, with a consistent number of axon branches
379 and large synaptic boutons (Menon et al., 2013). Wg signaling bidirectionally regulates
380 synaptic development, with *Wg* knockdown decreasing NMJ synaptic bouton number
381 and *Wg* overexpression (OE) increasing boutons (Packard et al., 2002; Kopke et al.,
382 2017), including an increase in satellite boutons (small boutons connected to the mature
383 (parent) bouton or adjacent axon; Torroja et al., 1999; Gatto and Broadie, 2008). To test
384 Cow requirements in synaptic architectural development, we labeled the wandering third
385 instar NMJ. Anti-horseradish peroxidase (HRP) was used to label the NMJ terminal by
386 binding to extracellular fucosylated N-glycans associated with the presynaptic neural
387 membrane (Jan and Jan, 1982; Parkinson et al., 2013). Anti-Discs Large (DLG) was
388 used to label the postsynaptic scaffold in the subsynaptic reticulum (Lahey et al., 1994;
389 Parnas et al., 2001). We used *cow*^{GDP}/*Df* (referred to as *cow* null) to eliminate *cow*
390 globally, and characterized *cow* RNAi lines (Chang and Sun, 2014) for both motor

391 neuron (*vglut-Gal4*) and muscle (*24B-Gal4*) cell-targeted knockdown studies. Sample
392 images and the summary of results are shown in Figure 3.

393 Cow restrains NMJ development, specifically restricting synaptic bouton formation.
394 When Cow is knocked out completely, there is a clear increase in boutons (Fig. 3A, left).
395 In quantified measurements, *cow* nulls show a very significant increase in synaptic
396 bouton number (w^{1118} 25.53 ± 1.37 vs. cow^{GDP}/Df 41.13 ± 1.6 ; $p < 0.0001$; Fig. 3A, right).
397 With targeted *cow* knockdown in presynaptic motor neurons (*vglut-Gal4 > cow-RNAi*),
398 there is the same increase in NMJ bouton formation (Fig. 3B), indicating Cow originates
399 from the neuron. Interestingly, presynaptic Cow knockdown also increases the number
400 of satellite boutons; (Fig. 3B; inset). Presynaptic *cow* knockdown causes very
401 significantly elevated mature bouton numbers (*vglut-Gal4/+* 26.69 ± 1.49 vs. *vglut > cow-*
402 *RNAi* 37.38 ± 1.75 ; $p = 0.0002$) as well as an increased percentage of satellite boutons
403 (*vglut-Gal4/+* $2.9 \pm 0.89\%$ vs. *vglut > cow-RNAi* 5.77 ± 1.86 ; $p = 0.061$; Fig. 3B, right).
404 Conversely, postsynaptic *cow* knockdown (*24B-Gal4 > cow-RNAi*) causes no discernable
405 differences from the controls (Fig. 3C, right). Mature and satellite bouton quantifications
406 demonstrate no effect of removing Cow from the muscle (mature; *24B/+* 30.63 ± 1.73 vs.
407 *24B > cow-RNAi* 28.06 ± 1.04 ; $p > 0.9999$; Fig. 3C, right; See Table 1 for satellite results).
408 Taken together, these results show Cow originating from the presynaptic motor neuron
409 restricts the formation of NMJ synaptic boutons.

410 When Cow is overexpressed (OE) in motor neurons (*vglut-Gal4 > UAS-Cow*), Cow
411 is elevated at the NMJ with a concomitant decrease in extracellular Wg ligand (Fig. 4A).
412 The NMJs have a typical number of mature boutons, but an increase in satellite boutons
413 (Fig. 4B). Interestingly, *cow* neuronal OE causes HRP redistribution with distinct spots

414 of accumulation (Fig. 4B, heatmap on right). Quantification shows a significant increase
415 in Cow levels secreted at the NMJ terminal (normalized *vglut-Gal4/+* 1.0 ± 0.06 vs.
416 *vglut>cow* 3.04 ± 0.06 ; $p<0.0001$), with a significant decrease in extracellular Wg levels
417 (*vglut-Gal4/+* 1.0 ± 0.08 vs. *vglut>cow* 0.67 ± 0.06 ; $p=0.001$; Fig. 4C). Quantification
418 shows no change in bouton number (*vglut-Gal4/+* 25.25 ± 0.81 vs. *vglut>Cow* 27.06 ± 1.4 ;
419 $P=0.27$), but a significant increase in satellite boutons (*vglut-Gal4/+* $2.33\pm 0.94\%$ vs.
420 *vglut>cow* 7.12 ± 0.67 ; $p=0.0003$; Fig. 4D). Whereas neuronal *cow* OE elevates normal
421 Cow expression at the NMJ, muscle *cow* OE causes aberrant, ectopic expression
422 (normalized *24B-Gal4/+* 1.0 ± 0.03 vs. *24B>cow* 3.91 ± 0.23 ; $p<0.0001$), which increases
423 Wg ligand (*24B-Gal4/+* 1.0 ± 0.07 vs. *24B>Cow* 1.52 ± 0.14 ; $p=0.003$). Muscle targeted
424 *cow* OE causes no change in mature boutons (*24B-Gal4/+* 30.38 ± 1.94 vs. *24B>cow*
425 29.81 ± 1.46 ; $P=0.82$) or the percentage of satellite boutons (*24B-Gal4/+* $3.16\pm 1.16\%$ vs.
426 *24B>cow* 5.48 ± 1.58 ; $P=0.2486$). We next assayed synaptic functional differentiation to
427 test if these structural changes have functional consequences.

428

429 **Cow restricts presynaptic vesicle fusion and neurotransmission strength**

430 We utilized two methods to assay NMJ synaptic functional differentiation and
431 neurotransmission strength: 1) two-electrode voltage-clamp (TEVC) electrophysiology
432 (Dani et al., 2012; Parkinson et al., 2013; Kopke et al., 2017), and 2) imaging genetically
433 encoded calcium reporter SynapGCaMP6f (Newman et al., 2017). For assaying evoked
434 transmission, muscle 6 was clamped (-60 mV) while the motor nerve was stimulated
435 with a suction electrode ($1.5\text{ mM } [Ca^{2+}]$). Excitatory junction current (EJC) traces were
436 recorded (0.2 Hz, 10 consecutive stimuli) to measure the average amplitude. For

437 assaying miniature EJC (mEJC) events, spontaneous synaptic vesicle fusions were
438 recorded, measuring frequency and amplitude. The mEJC frequency indicates
439 presynaptic vesicular release (number of active synapses, fusion probability), and
440 mEJC amplitude indicates number of activated postsynaptic receptors. For quantal
441 imaging, the SynapGCaMP reporter (*MHC-CD8-GCaMP6f-Sh*) contains a myosin heavy
442 chain (MHC) promoter for muscle targeting, CD8 transmembrane domain for membrane
443 targeting, and Shaker (Sh) K⁺ channel C-terminal tail for postsynaptic targeting
444 (Newman et al., 2017). By imaging transmission, we are able to specifically determine
445 the changes in quantal activity at the convergent motor neuron inputs separately. Live
446 imaging recordings were made of the SynapGCaMP reporter at muscle 4, with
447 spontaneous event frequency divided by the NMJ synaptic area, and event amplitude
448 measured as the change in the fluorescence signal over the baseline NMJ fluorescence
449 ($\Delta F/F_0$). Representative recordings and summarized data are shown in Figure 5.

450 With nerve stimulation, evoked transmission is clearly and consistently increased
451 in *cow* nulls compared to w^{1118} controls (Fig. 5A). Quantified measurements show EJC
452 amplitude significantly elevated (w^{1118} 175.4 \pm 9.93 nA vs. *cow*^{GDP} 214.6 \pm 12.24; $p=0.023$;
453 w^{1118} 175.4 \pm 9.93 vs. *cow*^{GDP}/*Df* 254.2 \pm 14.99; $p=0.012$; Fig. 5B). Although the *cow*^{GDP}/*Df*
454 mutants show a slight increase in mEJC frequency, no change was observed in the
455 *cow*^{GDP} nulls. We found no change in amplitude (Fig. 5C). In quantified measurements,
456 mEJC frequency is slightly increased in homozygous mutants and more increased in
457 the *cow*^{GDP}/*Df* (w^{1118} 1.396 \pm 0.19 Hz vs. *cow*^{GDP}/*cow*^{GDP} 1.764 \pm 0.23; $p=0.58$; w^{1118}
458 1.396 \pm 0.19 vs. *cow*^{GDP}/*Df* 2.41 \pm 0.49; $p=0.05$; Fig. 5D, left). There is no significant
459 change in mEJC amplitude (w^{1118} 0.75 \pm 0.03 nA vs. *cow*^{GDP}/*cow*^{GDP} 0.87 \pm 0.06; $p=0.189$;

460 w^{1118} 0.75 ± 0.03 nA vs. cow^{GDP}/Df 0.72 ± 0.05 ; $p=0.886$; Fig. 5D, right). Neuronally-
461 targeted cow -RNAi causes an increase in mEJC frequency ($vglut$ -Gal4/+ 1.5 ± 0.33 Hz
462 vs. $vglut > Cow$ -RNAi 2.45 ± 0.3 ; $p=0.045$), but not amplitude ($vglut$ -Gal4/+ 0.8 ± 0.03 nA
463 vs. $vglut > Cow$ -RNAi 0.85 ± 0.42 ; $p=0.4325$). SynapGCaMP imaging also shows
464 increased fusion frequency in type Ib boutons (Fig. 5E). In quantal imaging
465 measurements, spontaneous fusion frequency increases ($vglut$ -Gal4/+ 1.62 ± 0.47
466 Hz/ μm^2 vs. $vglut > cow$ -RNAi 2.98 ± 0.36 ; $p=0.051$; Fig. 5F, left). Interestingly, event
467 magnitude also significantly increases ($vglut$ -Gal4/+ 0.79 ± 0.04 $\Delta F/F_0$ vs. $vglut > cow$ -
468 RNAi 1.06 ± 0.09 ; $p=0.012$; Fig. 5F, right). These results demonstrate that Cow limits
469 evoked neurotransmission strength and suggest that neuronally secreted Cow regulates
470 synaptic vesicle fusion at the presynaptic active zone.

471

472 **Cow restricts presynaptic active zone and glutamatergic synapse formation**

473 We next used imaging to assay pre- and postsynaptic molecular components of
474 the synapse to test the hypothesis of increased NMJ synapse number in cow mutants.
475 The presynaptic active zone (AZ) is the specialized site of synaptic vesicle (SV) fusion
476 that mediates release of the glutamate neurotransmitter. Bruchpilot (Brp) tethers both
477 the voltage-gated Ca^{2+} channels and SVs to the AZ, and is the best AZ marker
478 (Hallermann et al., 2010). Each AZ directly apposes a postsynaptic glutamate receptor
479 (GluR) cluster to mediate fast neurotransmission (Schuster et al., 1991). We used co-
480 labeling with both anti-Brp (Wagh et al., 2006) and anti-GluRIIC (aka GluRIII; Marrus et
481 al., 2004) to compare cow null mutants to w^{1118} genetic background controls (Fig. 6).
482 Brp AZ punctae occur much more often in cow null NMJs (Fig. 6A), but are consistently

483 smaller in volume (Fig. 6B). In quantified measurements, the number of Brp AZ punctae
484 per NMJ is significantly increased in the *cow* null mutants compared to matched
485 controls (w^{1118} 193.1 ± 10.55 vs. cow^{GDP} 284.8 ± 10.54 ; $p < 0.0001$; Fig. 6A, right), but the
486 average volume of the Brp AZ synaptic punctae is significantly decreased in the
487 mutants (w^{1118} $0.86 \pm 0.033 \mu\text{m}^3$ vs. cow^{GDP} 0.72 ± 0.025 ; $p = 0.0019$; Fig. 6B, right). This is
488 consistent with a previous report also showing a reciprocal relationship between Brp AZ
489 punctae number and volume (Graf et al., 2009).

490 Brp AZ punctae are precisely juxtaposed to GluR clusters in a functional synapse
491 (Menon et al., 2013). For better resolution to image postsynaptic GluR clusters and
492 quantify the synaptic apposition, structured illumination microscopy (SIM) was employed
493 (Gustafsson, 2000). To compare to previous laser-scanning confocal imaging (LSM),
494 Brp AZs were first measured to find a consistent increase in the *cow* null mutants, but
495 with larger punctae numbers presumably due to increased resolution (w^{1118} 298.6 ± 17.2
496 vs. cow^{GDP} 387.9 ± 17.86 ; $p = 0.0019$; Fig. 6C). There is also a similar increase in GluR
497 clusters (w^{1118} 382 ± 23.21 vs. cow^{GDP} 542.8 ± 29.41 ; $p = 0.0004$; Fig. 6D). Brp punctae and
498 GluR clusters almost always partner, with rare exceptions seen at a similar frequency in
499 controls and mutants (Fig. 6D). There are more GluR clusters than Brp punctae in both
500 genotypes. The GluR/Brp ratio was measured to test for defects in synaptic apposition.
501 If there is a larger ratio in the mutants compared to controls, this would indicate more
502 GluR clusters without a Brp AZ. Conversely, a smaller ratio would indicate more GluR
503 clusters paired with a presynaptic partner. Quantified measurements show no difference
504 in the GluR/Brp ratio between controls and the *cow* null mutants (w^{1118} 1.29 ± 0.04 vs.

505 cow^{GDP} 1.36 ± 0.05 ; $p=0.272$). Taken together, these results demonstrate that Cow limits
506 NMJ synapse formation, consistent with strengthened neurotransmission.

507

508 **Membrane-tethering Wg prevents cow null defects in NMJ development**

509 Our starting hypothesis was that Cow regulates Wg by binding the ligand in the
510 extracellular space and carrying it across the synaptic cleft (from neuron to muscle).
511 This hypothesis is based on published work demonstrating that Cow is secreted, directly
512 binds secreted Wg, and acts to mediate intercellular transport (Chang and Sun, 2014).
513 To test this hypothesis, we obtained transgenic lines with the *wg* gene cut from its
514 native locus via FRT sites and then replaced either without (*FRT-wg*; transgenic control)
515 or with (*NRT-wg*) a membrane tether. Importantly, HA-tagged *NRT-wg* is not secreted
516 from Wg-expressing cells, and fails to maintain expression of long-range Wg targets
517 (Alexandre et al., 2014). We tested whether tethering Wg to the membrane affects NMJ
518 development. Comparing *FRT-wg* to *NRT-wg*, there is increased expression of the Wg
519 ligand around presynaptic boutons (data not shown). To determine if tethered Wg can
520 bind Fz2 receptors, NMJ bouton number was measured to assess presynaptic Wg
521 signaling. Next, *NRT-wg* was combined with the *cow* null mutant (*NRT-wg; cow^{GDP}*) to
522 test the hypothesis that Cow normally acts to regulate secreted Wg function. If Wg
523 needs to be secreted and transported dependent on Cow function, then *NRT-wg* and
524 *NRT-wg; cow^{GDP}* would be predicted to have the same phenotype. Representative
525 images and summarized data are shown in Figure 7.

526 In comparing the control *FRT-wg* and tethered *NRT-wg*, there is no change in
527 mature NMJ bouton number, but there is a clear increase in the number of immature

528 satellite boutons when Wg is tethered (Fig. 7A). In quantified measurements, *NRT-wg*
529 has the same number of NMJ synaptic boutons as the control (*FRT-wg* 26.71 ± 1.04 vs.
530 *NRT-wg* 27.04 ± 1.72 ; $p=0.999$; Fig. 7A,B), but a 4-fold increase in the percentage of
531 satellite boutons (*FRT-wg* $2.04 \pm 0.77\%$ vs. *NRT-wg* 8.3 ± 1.62 ; $p=0.0019$; Fig. 7C). When
532 membrane-tethered Wg is placed in the *cow* null background (*NRT-wg; cow^{GDP}*), both
533 the mature synaptic bouton number and the percentage of satellite boutons are similar
534 to the *FRT-wg* control levels (Fig. 7A). In quantified measurements, the mature bouton
535 number is no longer different between the two genotypes (*FRT-wg* 26.71 ± 1.04 vs. *NRT-*
536 *wg; cow^{GDP}* 26.78 ± 0.97 ; $p=0.999$; Fig. 7B; See Table 1 for all other comparisons), and
537 the satellite boutons are also restored to near normal levels (*FRT-wg* $2.04 \pm 0.77\%$ vs.
538 *NRT-wg; cow^{GDP}* 3.60 ± 1.1 ; $p=0.999$; Fig. 7C). Taken together, these results suggest
539 Cow facilitates Wg-dependent satellite bouton formation, and that Wg has to be
540 secreted for Cow to act on it. However, in contrast to the original hypothesis, Cow acts
541 as a negative regulator of secreted Wg signaling at the NMJ, suggesting that it should
542 interact with other Wg negative regulators in the extracellular synaptomatrix.

543

544 **Cow and Notum function together to restrict NMJ growth and bouton formation**

545 The secreted deacylase Notum has also been recently shown to regulate NMJ
546 synaptic bouton formation via the negative regulation of Wg *trans*-synaptic signaling
547 (Kopke et al., 2017). Notum restricts Wnt signaling by cleaving the Wg palmitoyl group
548 that binds to Fz2 receptors (Kakugawa et al., 2015). In *notum* null mutants, NMJ Wg
549 signaling is elevated both pre- and postsynaptically, resulting in increased synaptic
550 bouton number, synapse number and neurotransmission strength (Kopke et al., 2017).

551 To test the hypothesis that the increased NMJ development in *cow* null mutants is
552 similarly caused by an increase in Wg *trans*-synaptic signaling, we performed the
553 genetic test of combining *cow* and *notum* null heterozygotes to assay effects on NMJ
554 synaptic bouton development. The failure of mutant alleles at two different loci to
555 complement one another is one method to test for an *in vivo* interaction of the gene
556 products in a common signaling mechanism (nonallelic noncomplementation; Yook et
557 al., 2001; Hawley and Gilliland, 2006). In this case, the interaction tests the hypothesis
558 that Cow and Notum have closely associated functions in the regulation of Wg synaptic
559 signaling via direct interaction with the Wg ligand in the extracellular synaptomatrix. We
560 compared bouton formation in genetic background control (w^{1118}); *cow* null (cow^{GDP})
561 and *notum* null ($notum^{KO}$) homo- and heterozygotes; *cow/notum trans*-heterozygotes;
562 and *cow/notum* double null mutant ($cow^{GDP},notum^{KO}/cow^{GDP},notum^{KO}$). Representative
563 images and summarized data are shown in Figure 8.

564 The *trans*-heterozygote has a clearly expanded NMJ with more synaptic boutons
565 compared to controls, as well as other *wg* mutant phenotypes such as the appearance
566 of ghost boutons (Fig. 8A; inset). Ghost boutons are immature boutons that contain the
567 HRP marker, but do not yet contain the postsynaptic DLG protein (Ataman et al., 2006).
568 The *cow* ($cow^{GDP}/+$) and *notum* ($notum^{KO}/+$) heterozygotes alone are no different from
569 w^{1118} controls, and lack synaptic features of impaired Wg signaling (Fig. 8A; Table 1). In
570 quantified measurements, *trans*-heterozygotes have strongly increased bouton numbers
571 (w^{1118} 28.33±1.46 vs. $cow^{GDP}/notum^{KO}$ 46.13±1.08; $p<0.0001$; Fig. 8A, right; See Table
572 1 for all other comparisons). Extracellular Wg labeling without cellular permeabilization
573 in all these genotypes indicates no difference in the Wg fluorescence intensity (Fig. 8B).

574 In quantified measurements, there is no detectable change in Wg ligand levels between
575 controls and *cow/notum trans*-heterozygotes (normalized w^{1118} 1.0 ± 0.09 vs. $cow^{GDP/+}$;
576 $notum^{KO/+}$ 0.9 ± 0.09 ; $p=0.852$; Fig. 8B, right; See Table 1 for all other comparisons). The
577 double null mutants have significantly increased bouton numbers compared to controls
578 but no increase compared to each null alone (w^{1118} 22.94 ± 1.05 vs. cow^{GDP} ,
579 $notum^{KO}/cow^{GDP}$, $notum^{KO}$ 29.13 ± 0.97 ; $p=0.0005$; Fig. 8C, right; See Table 1 for all other
580 comparisons). Interestingly, *trans*-heterozygotes show no change in nerve-stimulation
581 evoked EJC recordings (See Table 1). These results indicate Cow and Notum act in the
582 same pathway to restrict Wg signaling in structural development, and that the level of
583 extracellular Wg ligand alone is not predictive of signaling activity.

584

585 Discussion

586 The function of signaling ligands in the extracellular space is tightly regulated to
587 ensure coordinated intercellular development, often via glycan-dependent mechanisms
588 (Dani and Broadie, 2012; Parkinson et al., 2013; Shilts and Broadie, 2017). The most
589 recently discovered *Drosophila* HSPG, secreted Cow, was characterized with this role
590 (Chang and Sun, 2014). In the developing wing disc, the Wnt Wg is produced in a stripe
591 of cells at the dorsal/ventral margin boundary, and acts as an intercellular morphogen
592 through Fz2 receptor signaling (Zecca et al., 1996; Bhanot et al., 1996; Neumann and
593 Cohen, 1997). The glypican HSPGs Dally and Dally-like (Dlp), bound to outer plasma
594 membrane leaflets via GPI anchors, bind Wg to regulate both ligand distribution and
595 intercellular signaling (Tsuda et al., 1999; Baeg et al., 2001; Dani et al., 2012; Dear et
596 al., 2017). It has been proposed that Dally/Dlp HSPGs are involved in the movement of

597 extracellular Wg to form a morphogen gradient (Han et al., 2005). However, in *dally dlp*
598 double mutant clones, extracellular Wg is detected far away from Wg-secreting cells,
599 suggesting another extracellular factor can transport Wg. Cow was shown to fill this role
600 by binding extracellular Wg to increase stability and rate of movement from producing to
601 receiving cells (Chang and Sun, 2014). Supporting this model, *cow* mutants manifest
602 Wg ligand gain-of-function (GOF)/overexpression phenotypes for short-range targets,
603 and loss-of-function (LOF) phenotypes for long-range targets.

604 At the NMJ, such a long-range Wg morphogen transport function is not seemingly
605 required, except perhaps as a clearance mechanism, but Wg extracellular regulation
606 and short-range Wg transport to cross the synaptic cleft is critical for NMJ development
607 (Packard et al., 2002; Friedman et al., 2013; Dear et al., 2016; Parkinson et al., 2016).
608 At the forming NMJ, Wg from neurons and glia signals both presynaptically (neuronal)
609 and postsynaptically (muscle) via Fz2 receptors (Packard et al., 2002; Kerr et al., 2014).
610 In the motor neuron, Wg signaling inhibits the glycogen synthase kinase 3 β (GSK3 β)
611 homolog Shaggy (Sgg) to regulate the microtubule-associated protein 1B (MAP1B)
612 homolog Futsch to modulate microtubule dynamics controlling NMJ bouton formation
613 (Miech et al., 2008). However, Futsch distribution and microtubule dynamics do not
614 change with elevated Wg signaling (Kopke et al., 2017), so this pathway alone does not
615 explain the increased bouton formation with increased Wg signaling. In the postsynaptic
616 muscle, Wg signaling drives Fz2 endocytosis and C-terminus cleavage, with transport to
617 the nucleus regulating mRNAs involved in synaptogenesis, including postsynaptic GluR
618 distribution (Speese et al., 2012). In *wg* mutants, GluRs are more diffuse; with clusters
619 irregular in size/shape, increased receptor numbers and a larger postsynaptic volume

620 (Packard et al., 2002; Speese et al., 2012; Kerr et al., 2014). Thus, Wg *trans*-synaptic
621 signaling controls both NMJ structure and function.

622 Based on the findings from Chang and Sun (2014), we hypothesized that Cow
623 binds Wg to facilitate the transport across the synapse to Fz2 receptors on the muscle.
624 If this is correct, we would expect a presynaptic Wg overexpression (OE) phenotype in
625 the absence of Cow (Wg buildup at the source), and a postsynaptic Wg decrease/loss
626 phenotype (failure of Wg transport). Presynaptically, we find increased synaptic bouton
627 number in *cow* null mutants phenocopying the Wg OE condition (Kopke et al., 2017),
628 consistent with this hypothesis. These results indicate that Cow normally inhibits NMJ
629 bouton formation, consistent with the effects of inhibiting presynaptic Wg signaling
630 (Packard et al., 2002). Postsynaptically, we find an increased number of GluR clusters
631 due to elevated synapse formation in *cow* null mutants, but no evidence of diffuse GluR
632 clusters of irregular size/shape and larger volume as has been reported in *wg* mutants
633 (Packard et al., 2002; Speese et al., 2012; Kerr et al., 2014). Therefore, we do not find
634 strong support for the second prediction of the hypothesis. GluR changes within single
635 postsynaptic domains are challenging to see even with enhanced resolution microscopy
636 (such as the structured illumination microscopy (SIM) used here; Gustafsson, 2000), but
637 future studies could focus more on GluRIIA cluster size/shape/intensity in *cow* mutants.
638 If GluR defects are detected in *cow* nulls, it would be interesting to test the Frizzled
639 Nuclear Import (FNI) pathway (Mathew et al., 2005).

640 Wg signaling regulates multiple steps of NMJ development including branching,
641 satellite bouton budding and synaptic bouton maturation (Koles and Budnik, 2012).
642 None of the *cow* manipulations cause changes in branching, indicating Cow does not

643 regulate this Wg signaling, likely working in concert with other Wg regulators. Wg loss
644 (*wg^{ts}*) decreases bouton formation (Packard et al., 2002), while neural Wg OE increases
645 branching, satellite and total bouton numbers (Packard et al., 2002; Miech et al., 2008;
646 Kopke et al., 2017). Satellite boutons represent an immature stage of development, with
647 small boutons connected to the mature (parent) bouton or adjacent axon (Torroja et al.,
648 1999; Gatto and Broadie, 2008). Neuronal Cow OE does not change mature bouton
649 number, but increases satellite bouton budding. Neuronal Cow RNAi also increases
650 satellite boutons. Thus, changing neural Cow levels in either direction elevates satellite
651 bouton numbers, suggesting different consequences on budding versus developmental
652 arrest. It also appears that the cellular source of secreted Cow, or the balance between
653 sources, may be important for proper Wg regulation. Importantly, glia-secreted Wg
654 regulates distinct aspects of synaptic development (Kerr et al., 2014), with loss of glial-
655 derived Wg accounting for some, but not all, of *wg* mutant phenotypes. Similarly, cell-
656 targeted *cow* manipulations cause different NMJ phenotypes. There is no evidence for
657 normal Cow function in postsynaptic muscle, but it remains possible that Cow secreted
658 from glia could regulate Wg *trans*-synaptic signaling.

659 Increasing Wg signaling elevates evoked transmission strength and functional
660 synapse number (Kopke et al., 2017), which is phenocopied in *cow* null mutants. Block
661 of postsynaptic Wg signaling causes increased SV fusion frequency and amplitude of
662 miniature excitatory junctional potentials (Speese et al., 2012). With neuronal *cow* RNAi,
663 there is a similar increase in event frequency and amplitude. These results suggest a
664 decrease in postsynaptic Wg signaling when *cow* is lost, supporting the Wg transport
665 hypothesis. Blocking Wg secreted from neurons or glia increases muscle GluR cluster

666 size, albeit with differential effects on neurotransmission efficacy (Kerr et al., 2014).
667 Reducing neuronal Wg has no effect on mEJC frequency, but reducing glial-derived Wg
668 increases SV fusion frequency (Kerr et al., 2014). Both nerve-evoked and spontaneous
669 neurotransmission are increased in *cow* null mutants, together with increased Brp active
670 zones and postsynaptic GluR clusters forming supernumerary synapses. SynapGCaMP
671 is an exciting new tool to test function at individual synapses (Newman et al., 2017).
672 With targeted neuronal *cow* RNAi, there is an increase in both the number of SV fusion
673 events and the postsynaptic Ca^{2+} signal amplitude, consistent with both presynaptic and
674 postsynaptic regulation of Wg signaling (Packard et al., 2002; Speese et al., 2012; Kerr
675 et al., 2014). These functional phenotypes, combined with coordinated changes in pre-
676 and postsynaptic formation suggest Cow regulates *trans*-synaptic Wg transport.

677 There were differences between spontaneous synaptic vesicle fusion findings
678 between TEVC electrophysiological recordings and SynapGCaMP reporter (*MHC-CD8-*
679 *GCaMP6f-Sh*) Ca^{2+} imaging (Newman et al., 2017). Motor neuron presynaptically
680 targeted *cow* RNAi showed stronger impacts on SV fusion frequency with imaging in
681 contrast to recordings, comparable to effects in the *cow*^{GDP} null mutants. Moreover,
682 SynapGCaMP imaging revealed significantly larger SV fusion event magnitudes in
683 contrast to the lack of change found with TEVC recording. While the basis of these
684 differences is unknown, we speculate that it is due to the differential nature or sensitivity
685 of these two methods. The Ca^{2+} imaging is based on measuring the change in the
686 fluorescence signal over the baseline NMJ fluorescence ($\Delta F/F_0$; Newman et al., 2017),
687 and it may be that glutamate receptor Ca^{2+} permeability or intracellular Ca^{2+} signaling
688 dynamics is changed in a way not directly related to detectable membrane current

689 changes in the *cow* mutants. TEVC recordings capture whole NMJ activity, whereas
690 with imaging we only captured type 1b bouton activity normalized to area. In future
691 studies, SynapGCaMP imaging can be used to map spatial changes in synapse
692 function by assaying quantal activity separately in convergent type 1s and 1b motor
693 neuron inputs and within discrete synaptic boutons (Newman et al., 2017). Moreover,
694 differences between *cow*^{GDP} and *cow*^{GDP}/*Df* conditions could be influenced by second-
695 site enhancing mutations on the *Df* chromosome. Overall, it should be noted that the
696 changes in spontaneous SV fusion frequency and amplitude in *cow* mutants are subtle
697 and variable, and need to be further studied in the future.

698 Wg is lipid-modified via palmitoylation to become strongly membrane associated
699 (Zhai et al., 2004). The hydrophobic moiety is located at the interface of Wg and Fz2
700 binding, shielded from the aqueous environment by multiple extracellular transporters
701 until signaling interaction with the receptor (Takada et al., 2017). There have been many
702 modes of extracellular Wg transport demonstrated, primarily from work in the wing disc,
703 including microvesicles, lipoproteins, exosomes and cytoneme membrane extensions
704 (Greco et al., 2001; Panáková et al., 2005; Gross et al., 2012; Huang and Kornberg,
705 2015). These multiple mechanisms of transport are much less studied at the synapse;
706 however, exosome-like vesicles containing the Wg-binding protein Evenness
707 Interrupted (*Evi*) have been demonstrated at the *Drosophila* NMJ (Korkut et al., 2009).
708 *Cow* could be considered an alternative extracellular Wg transport method (Chang and
709 Sun, 2014), acting to shield Wg while facilitating transport through the extracellular
710 synaptomatrix (Dani and Broadie, 2012; Dear et al., 2016). In addition, HSPGs have
711 been shown to regulate ligands by stabilizing, degrading or sequestering the ligand, or

712 as bifunctional co-receptors, or facilitators of transcytosis (Lin, 2004; Dani et al., 2012;
713 Dear et al., 2017). Results presented here are consistent with the hypothesis that Cow
714 is mediating Wg transport across the NMJ synapse (Chang and Sun, 2014), but also
715 that Cow has an additional role in the negative regulation of Wg synaptic signaling.

716 The need for secreted Wg has been recently challenged, with Wg tethering to the
717 membrane (*NRT-wg*) showing Wg secretion to be largely dispensable for development
718 (Alexandre et al., 2014). In contrast, other recent studies suggest that Wg release and
719 spreading is necessary (Beaven and Denholm, 2018; Pani and Goldstein, 2018; Stewart
720 et al., 2019). We find tethering Wg at the NMJ synapse increases extracellular Wg
721 ligand levels, with no change in mature bouton numbers. This Wg accumulation shows
722 *NRT-wg* is more stable at the synaptic signaling interface, consistent with other studies
723 (Morata and Struhl, 2014; Chaudhary and Boutros, 2018). However, even though Wg
724 levels increase, Wg signaling is less effective. With *NRT-wg*, only the budding of new
725 satellite bouton is increased, with no increase in mature bouton formation. Reducing Wg
726 function causes Fz2 upregulation (Cadigan et al., 1998; Chaudhary and Boutros, 2018),
727 so we hypothesize Wg signaling could be maintained by increased presynaptic Fz2
728 receptors. When Wg is tethered, Cow cannot mediate intercellular transport, so the
729 hypothesis predicts similar phenotype with (*NRT-wg*) or without Cow (*NRT-wg; cow^{GDP}*).
730 Indeed, Cow removal in the *NRT-wg* condition does not impact synaptic bouton number,
731 although it does block the increase in satellite boutons, consistent with a Cow role in
732 greater Wg stability (Chang and Sun, 2014). These results show that Wg secretion is
733 required for the elevated NMJ development characterizing *cow* mutant animals.

734 To further test how Cow is working through the Wg pathway to negatively regulate
735 NMJ development, we turned to genetic interaction tests with the Wg negative regulator
736 Notum (Gerlitz and Basler, 2002; Giráldez et al., 2002; Kakugawa et al., 2015). At the
737 NMJ, Wg *trans*-synaptic signaling is elevated in the absence of Notum, and null *notum*
738 mutants display larger NMJs with more synaptic boutons, increased synapse number
739 and elevated neurotransmission (Kopke et al., 2017). All these defects are phenocopied
740 by neuronal Wg OE, showing that the positive synaptogenic phenotypes arise from lack
741 of Wg signaling inhibition. Consistently, genetically correcting Wg levels at the synapse
742 in *notum* nulls alleviates synaptogenic phenotypes (Kopke et al., 2017). We show here
743 that *cow* null mutants have the same phenotypes of expanded NMJs, supernumerary
744 synaptic boutons, greater synapse number/function and strengthened transmission,
745 suggesting Cow acts like Notum in regulating Wg signaling. We performed a genetic
746 test to ask whether Cow and Notum work in this same pathway. While *cow* and *notum*
747 null heterozygotes do not exhibit NMJ defects, *cow/notum trans*-heterozygotes display
748 grossly expanded NMJs with excess boutons. This combined haplo-insufficiency (type 3
749 SSNC) of nonallelic noncomplementation suggests Cow and Notum share related roles
750 (Yook et al., 2001; Hawley and Gilliland, 2006). When we tested full double mutants,
751 there is no additive effect, showing that Cow and Notum restrict Wg signaling in the
752 same pathway. However, this pathway convergence appears restricted only to the
753 control of structural synaptogenesis but not functional neurotransmission, although the
754 control neurotransmission amplitude was elevated in these studies.

755 Cow now joins the list of synaptic HSPGs with key roles in NMJ development.
756 HSPGs have been implicated in vertebrate NMJ synapse formation for >3 decades

757 (Kamimura and Maeda, 2017; Condomitti and Wit, 2018). The Agrin HSPG is secreted
758 from presynaptic terminals to maintain postsynaptic acetylcholine receptor clustering
759 (Godfrey et al., 1984; Hubbard et al., 2013). Another secreted HSPG, Perlecan,
760 regulates acetylcholinesterase localization (Peng et al., 1999; Arikawa-Hirasawa et al.,
761 2002). *Drosophila* NMJ analyses have begun to more systematically elucidate HSPG
762 roles in NMJ formation and function (Ren et al., 2009; Kamimura and Maeda, 2017). In
763 particular, the glypican HSPG Dlp regulates Wg signaling to modulate both NMJ
764 structure and function, including the regulation of active zone formation and SV release
765 (Johnson et al., 2006; Dani et al., 2012; Friedman et al., 2013; Dear et al., 2017). Wg
766 binds the core Dlp protein, with HS chains enhancing this binding, to retain Wg on the
767 cell surface, where it can both compete with Fz2 receptors and facilitate Wg-Fz2 binding
768 (Yan et al., 2009). This biphasic activity depends on the ratio of Wg, Fz2 and Dlp HSPG
769 as expounded in 'exchange factor model' (Yan et al., 2009; Dear et al., 2016). Cow may
770 impact this exchange factor mechanism as a fourth player, acting with Dlp to modulate
771 Wg transport and Wg-Fz2 binding at the synaptic interface. It will be important to test
772 Dlp levels and distribution in *cow* nulls to see how Cow fits into this model.

773 In addition to Cow, Perlecan (Trol) is another secreted HSPG reported to regulate
774 bidirectional Wg signaling at the *Drosophila* NMJ (Kamimura et al., 2013). Trol has been
775 localized near the muscle membrane, where it promotes postsynaptic Wg accumulation.
776 In the absence of Trol, Wg builds up presynaptically, causing excess satellite bouton
777 formation (Kamimura et al., 2013). It is interesting to note that *cow* mutants enhance Wg
778 signaling without increasing satellite boutons. In *trol* mutants, ghost boutons increase
779 due to decreased postsynaptic Wg signaling (Kamimura et al., 2013). Note that cow

780 mutants do not exhibit ghost boutons, which fails to support decreased postsynaptic Wg
781 signaling. Other postsynaptic defects in *trol* mutants (e.g. reduced subsynaptic reticulum
782 (SSR), increased postsynaptic pockets; Kamimura et al., 2013) are NMJ ultrastructural
783 features that could be a future focus using electron microscopy studies. Similar to *cow*
784 mutants, extracellular Wg levels are decreased in the absence of *Trol*, speculated due
785 to increased Wg proteolysis, since HS protects HS-binding proteins from degradation
786 (Saksela et al., 1988). In *cow* mutants, it is not yet known whether Wg is decreased due
787 to elevated signaling (ligand/receptor endocytosis), or increased degradation due to
788 *Cow* no longer protecting/stabilizing the ligand. Given synaptic Fz2 is internalized with
789 Wg binding (Mathew et al., 2005), future experiments could test internalized Fz2 levels
790 in *cow* mutants as a proxy of Wg signaling.

791 In summary, we have confirmed here new tools to study *Cow* HSPG function,
792 and discovered *Cow* from presynaptic motor neurons restricts NMJ bouton formation,
793 glutamatergic synapse number and NMJ functional differentiation. *Cow* acts within the
794 same Wg *trans*-synaptic signaling pathway as Notum by regulating the Wg ligand in the
795 extracellular synaptomatrix. Secreted *Cow* modulates extracellular Wg ligand levels,
796 with additional functions controlling Wg signaling efficacy, which may be independent or
797 dependent of Wg transport. It will be interesting to determine whether *Cow* core protein
798 and/or its HS chains are important for the synaptic structural and functional phenotypes.
799 Wg must be secreted for *Cow* to act on it, as shown by the membrane-tethered
800 interaction studies, showing secreted *Cow* must work on the freely-diffusible Wg ligand.
801 Perhaps most informative for our future studies will be dissection of the interactions,
802 coordination or redundancy of the multiple synaptic HSPGs at the NMJ, to further the

803 understanding of extracellular Wg *trans*-synaptic signaling regulation during synaptic
804 development. *Drosophila* is particularly well-suited model to study HSPGs owing to the
805 relatively reduced complexity in this system (17 HSPGs in mammals vs. 5 in *Drosophila*;
806 Sarrazin et al., 2011). We look forward to expanding future studies to examine multiple
807 synaptic HSPGs in parallel, with the goal of elucidating the surprisingly complex control
808 of *trans*-synaptic signaling occurring within the extracellular synaptomatrix.

809 **References**

810 Alexandre C, Baena-Lopez A, Vincent J-P (2014) Patterning and growth control by
811 membrane-tethered Wingless. *Nature* 505(7482):180-5.

812

813 Arikawa-Hirasawa E, Rossi SG, Rotundo RL, Yamada Y (2002) Absence of
814 acetylcholinesterase at the neuromuscular junctions of perlecan-null mice. *Nat Neurosci*
815 5:119-23.

816

817 Ataman B, Ashley J, Gorczyca D, Gorczyca M, Mathew D, Wichmann C, Sigrist SJ,
818 Budnik V (2006) Nuclear trafficking of *Drosophila* Frizzled-2 during synapse
819 development requires the PDZ protein dGRIP. *PNAS* 103(20):7841-46.

820

821 Ataman B, Ashley J, Gorczyca M, Ramachandran P, Fouquet W, Sigrist SJ, Budnik V
822 (2008) Rapid Activity-Dependent Modifications in Synaptic Structure and Function
823 Require Bidirectional Wnt Signaling. *Neuron* 57(5):705-18.

824

825 Baeg GH, Lin X, Khare N, Baumgartner S, Perrimon N (2001) Heparan sulfate
826 proteoglycans are critical for the organization of the extracellular distribution of
827 Wingless. *Development* 128:87-94.

828

829 Beaven R, Denholm B (2018) Release and spread of Wingless is required to pattern the
830 proximo-distal axis of *Drosophila* renal tubules. *eLIFE* 7:e35373.

831

832 Bellen HJ, Levis RW, Liao G, He Y, Carlson JW, Tsang G, Evans-Holm M, Hiesinger
833 PR, Schulze KL, Rubin GM, Hoskins RA, Spralding AC (2004) The BDGP Gene
834 Disruption Project: Single Transposon Insertions Associated With 40% of *Drosophila*
835 Genes. *Genetics* 167:761-81.

836

837 Bhanot P, Brink M, Samos CH, Hsieh J-C, Wang Y, Macke JP, Andrew D, Nathans J,
838 Nusse R (1996) A new member of the *frizzled* family from *Drosophila* functions as a
839 Wingless receptor. *Nature* 382:225-30.

840

841 Cadigan KM, Fish MP, Rulifson EJ, Nusse R (1998) Wingless Repression of *Drosophila*
842 *frizzled 2* Expression Shapes the Wingless Morphogen Gradient in the Wing. *Cell*
843 93(5):767-77.

844

845 Chang Y-H, Sun YH (2014) Carrier of Wingless (Cow), a Secreted Heparan Sulfate
846 Proteoglycan, Promotes Extracellular Transport of Wingless. *PLoS ONE* 9(10):e111573.

847

848 Chaudhary V, Hingole S, Frei J, Port F, Strutt D, Boutros M (2019) Robust Wnt
849 signaling is maintained by a Wg protein gradient and Fz2 receptor activity in the
850 developing *Drosophila* wing. *Development* 146(15):dev174789.

851

852 Condomitti G, de Wit J (2018) Heparan Sulfate Proteoglycans as Emerging Players in
853 Synaptic Specificity. *Front Mol Neurosci* 11:14.

854

855 Dani N, Broadie K (2012) Glycosylated synaptomatrix regulation of trans-synaptic
856 signaling. *Dev Neurobiol* 72(1):2-21.

857

858 Dani N, Nahm M, Lee S, Braodie K (2012) A Targeted Glycan-Related Gene Screen
859 Reveals Heparan Sulfate Proteoglycan Sulfation Regulates WNT and BMP Trans-
860 Synaptic Signaling. *PLoS Genetics* 8(11):e1003031.

861

862 Dear ML, Dani N, Parkinson W, Zhou S, Broadie K (2016) Two classes of matrix
863 metalloproteinases reciprocally regulate synaptogenesis. *Development* 143(1):75-87.

864

865 Dear ML, Shilts J, Broadie K (2017) Neuronal activity drives FMRP- and HSPG-
866 dependent matrix metalloproteinase function required for rapid synaptogenesis. *Sci*
867 *Signal* 10(504):eaan3181.

868

869 Franco B, Bogdanik L, Bobinnec Y, Debec A, Bockaert J, Parmentier M-L, Grau Y
870 (2004) Shaggy, the Homolog of Glycogen Synthase Kinase 3, Controls Neuromuscular
871 Junction Growth in *Drosophila*. *J Neurosci* 24(29):6573-7.

872

873 Friedman S, Dani N, Rushton E, Broadie K (2013) Fragile X mental retardation protein
874 regulates trans-synaptic signaling in *Drosophila*. *Dis Model Mech* 6(6):1400-13.

875

876 Gatto CL, Broadie K (2008) Temporal requirements of the fragile X mental retardation
877 protein in the regulation of synaptic structure. *Development* 135:2637-48.

878

879 Gerlitz O, Basler K (2002) Wingful, an extracellular feedback inhibitor of Wingless.

880 Genes Dev 16(9):1055-9

881

882 Giráldez AJ, Copley RR, Cohen SM (2002) HSPG Modification by the Secreted Enzyme

883 Notum Shapes the Wingless Morphogen Gradient. Cell 2(5):667-76.

884

885 Godfrey EW, Nitkin RM, Wallace BG, Rubin LL, McMahan UJ (1984) Components of

886 Torpedo electric organ and muscle that cause aggregation of acetylcholine receptors on

887 cultured muscle cells. JCB 99(2):615-27.

888

889 Graf ER, Daniels RW, Burgess RW, Schwarz TL, DiAntonio A (2009) Rab3 Dynamically

890 Controls Protein Composition at Active Zones. Neuron 64(5):663-77.

891

892 Greco V, Hannus M, Eaton S (2001) Argosomes: A Potential Vehicle for the Spread of

893 Morphogens through Epithelia. Cell 106(5):633-45.

894

895 Gross JC, Chaudhary V, Bartscherer K, Boutros M (2012) Active Wnt proteins are

896 secreted on exosomes. Nat Cell Biol 435(7038):58-65.

897

898 Gustafsson MGL (2000) Surpassing the lateral resolution limit by a factor of two using

899 structured illumination microscopy. J Microsc 198(2):82-7.

900

- 901 Hallermann S, Kittel RJ, Wichmann C, Weyhersmüller A, Fouquet W, Mertel S, Oswald
902 D, Eimer S, Depner H, Schwärzel M, Sigrist SJ, Heckmann M (2010) Naked Dense
903 Bodies Provoke Depression. *J Neurosci* 30(43):14340-45.
904
- 905 Han C, Yan D, Belenkaya TY, Lin X (2005) *Drosophila glypicans* Dally and Dally-like
906 shape the extracellular Wingless morphogen gradient in the wing disc. *Development*
907 132(4):667-79.
908
- 909 Hawley RS, Gilliland WD (2006) Sometimes the result is not the answer: the truths and
910 the lies that come from using the complementation test. *Genetics* 174(1):5-15.
911
- 912 Huang H, Kornberg TB (2015) Myoblast cytonemes mediate Wg signaling from the wing
913 imaginal disc and Delta-Notch signaling to the air sac primordium. *eLIFE* 4:e06114.
914
- 915 Hubbard SR, Gnanasambandan K (2013) Structure and activation of MuSK, a receptor
916 tyrosine kinase central to neuromuscular junction formation. *Biochim Biophys Acta*
917 1834(10):2166-2169.
918
- 919 Jan LY, Jan YN (1982) Antibodies to horseradish peroxidase as specific neuronal
920 markers in *Drosophila* and in grasshopper embryos. *PNAS* 79(8):2700-4.
921
- 922 Johnson KG, Tenney AP, Ghose A, Duckworth AM, Higashi ME, Parfitt K, Marcu O,
923 Heslip TR, Marsh JL, Schwarz TL, Flanagan JG, Van Vactor D (2006) The HSPGs

924 Syndecan and Dallylike Bind the Receptor Phosphatase LAR and Exert Distinct Effects
925 on Synaptic Development. *Neuron* 49(4):517-31.

926

927 Kakugawa S, Langton PF, Zebisch M, Howell SA, Chang T-H, Liu Y, Feizi T, Bineva G,
928 O'Reilly N, Snijders AP, Jones EY, Vincent J-P (2015) Notum deacylates Wnt proteins
929 to suppress signalling activity. *Nature* 519(7542):187-92.

930

931 Kamimura K and Maeda N (2017) Heparan sulfate proteoglycans in *Drosophila*
932 neuromuscular development. *Biochim Biophys Acta* 1861(10):2442-6.

933

934 Kamimura K, Ueno K, Nakagawa J, Hamada R, Saitoe M, Maeda N (2013) Perlecan
935 regulates bidirectional Wnt signaling at the *Drosophila* neuromuscular junction. *JCB*
936 200(2):219.

937

938 Kerr KS, Fuentes-Medel Y, Brewer C, Barria R, Ashley J, Abruzzi KC, Sheehan A,
939 Tasdemir-Yilmaz OE, Freeman MR, Budnik V (2014) Glial Wingless/Wnt Regulates
940 Glutamate Receptor Clustering and Synaptic Physiology at the *Drosophila*
941 Neuromuscular Junction. *J Neurosci* 34(8):2910-20.

942

943 Koles K, Budnik V (2012) Wnt Signaling in Neuromuscular Junction Development. *Cold*
944 *Spring Harb Perspect Biol* 4:a008045.

945

946 Kopke DL, Lima SC, Alexandre C, Broadie K (2017) Notum coordinates synapse
947 development via extracellular regulation of Wingless trans-synaptic signaling.
948 Development 144(19):3499-510.

949

950 Korkut C, Ataman B, Ramachandran P, Ashley J, Barria R, Cherbesi N, Budnik V
951 (2009) Trans-Synaptic Transmission of Vesicular Wnt Signals through Evi/Wntless. Cell
952 139(2):393-404.

953

954 Kittel RJ, Wichmann C, Rasse TM, Fouquet W, Schmidt M, Schmid A, Wagh DA, Pawlu
955 C, Kellner RR, Willig KI, Hell SW, Buchner E, Heckmann M, Sigrist SJ (2006) Bruchpilot
956 Promotes Active Zones Assembly, Ca²⁺ Channel Clustering, and Vesicle Release.
957 Science 312(5776):1051-4.

958

959 Lahey T, Gorczyca M, Jia X-X, Budnik V (1994) The drosophila tumor suppressor gene
960 *dlg* is required for normal synaptic bouton structure. Neuron 13(4):823-35.

961

962 Lin X (2004) Functions of heparan sulfate proteoglycans in cell signaling during
963 development. Development 131(24):6009-21.

964

965 Marrus SB, Portman SL, Allen MJ, Moffat KG, DiAntonio A (2004) Differential
966 Localization of Glutamate Receptor Subunits at the *Drosophila* Neuromuscular Junction.
967 J Neurosci 24(6):1406-15.

968

969 Masu M (2016) Proteoglycans and axon guidance: a new relationship between old
970 partners. *J Neurochem* 139(2):58-75.

971

972 Mathew D, Ataman B, Chen J, Zhang Y, Cumberledge S, Budnik V (2005) Wingless
973 signaling at synapses is through cleavage and nuclear import of receptor DFrizzled2.
974 *Science* 310(5752):1344-7.

975

976 Menon KP, Carrillo RA, Zinn K (2013) Development and plasticity of the *Drosophila*
977 larval neuromuscular junction. *WIREs Dev Biol* 2:647-70.

978

979 Miech C, Pauer H-U, He X, Schwarz TL (2008) Presynaptic Local Signaling by a
980 Canonical Wingless Pathway Regulates Development of the *Drosophila* Neuromuscular
981 Junction. *J Neurosci* 28(43):10875-84.

982

983 Morata G and Struhl G (2014) Tethered wings. *Nature* 505:162-3.

984

985 Nagarkar-Jaiswal S, Lee P-T, Campbell ME, Chen K, Anguiano-Zarate S, Gutierrez MC,
986 Busby T, Lin W-W, He Y (2015) A library of MiMICs allows tagging of genes and
987 reversible, spatial and temporal knockdown of proteins in *Drosophila*. *eLIFE* 4:e05338.

988

989 Neumann CJ, Cohen SM (1997) Long-range action of Wingless organizes the dorsal-
990 ventral axis of the *Drosophila* wing. *Development* 124:871-80.

991

992 Newman ZL, Hoagland A, Aghi K, Worden K, Levy SL, Son JH, Lee LP, Isacoff EY
993 (2017) Input-Specific Plasticity and Homeostasis at the *Drosophila* Larval
994 Neuromuscular Junction. *Neuron* 93(6):1388-404.

995

996 Packard M, Koo ES, Gorczyca, Sharpe J, Cumberledge S, Budnik V (2002) The
997 *Drosophila* Wnt, wingless, provides an essential signal for pre- and postsynaptic
998 differentiation. *Cell* 111(3):319-30.

999

1000 Panáková D, Sprong H, Marois E, Thiele C, Eaton S (2005) Lipoprotein particles are
1001 required for Hedgehog and Wingless signaling. *Nature* 435(7038):58-65.

1002

1003 Pani AM, Goldstein B (2018) Direct visualization of a native Wnt in vivo reveals that a
1004 long-range Wnt gradient forms by extracellular dispersal. *eLIFE* 7:e38325.

1005

1006 Parkinson W, Dear ML, Rushton E, Broadie K (2013) N-glycosylation requirements in
1007 neuromuscular synaptogenesis. *Development* 140(24):4970-81.

1008

1009 Parkinson WM, Dookwah M, Dear ML, Gatto CL, Aoki K, Tiemeyer M, Broadie K (2016)
1010 Synaptic roles for phosphomannomutase type 2 in a new *Drosophila* congenital disorder
1011 of glycosylation disease model. *Dis Model Mech* 9:513-27.

1012

1013 Parnas D, Haghghi AP, Fetter RD, Kim SW, Goodman CS (2001) Regulation of
1014 Postsynaptic Structure and Protein Localization by the Rho-Type Guanine Nucleotide
1015 Exchange Factor dPix. *Neuron* 32(3):415-24.

1016

1017 Peng HB, Xie H, Rossi SG, Rotundo RL (1999) Acetylcholinesterase Clustering at the
1018 Neuromuscular Junction Involves Perlecan and Dystroglycan. *JCB* 145(4):911.

1019

1020 Ren Y, Kirkpatrick CA, Rawson JM, Sun M, Selleck SB (2009) Cell Type-Specific
1021 Requirements for Heparan Sulfate Biosynthesis at the *Drosophila* Neuromuscular
1022 Junction: Effects on Synapse Function, Membrane Trafficking, and Mitochondrial
1023 Localization. *J Neurosci* 29(26):8539-50.

1024

1025 Saksela O, Moscatelli D, Sommer A, Rifkin DB (1988) Endothelial cell-derived heparan
1026 sulfate binds basic fibroblast growth factor and protects it from proteolytic degradation. *J*
1027 *Cell Biol* 107(2):743-51.

1028

1029 Sarrazin S, Lamanna WC, Esko JD (2011) Heparan Sulfate Proteoglycans. *Cold Spring*
1030 *Harb Perspect Biol* 3(7):a004952.

1031

1032 Schnepf A, Lindgren PK, Hülsmann H, Kröger S, Paulsson M, Hartmann U (2005)
1033 Mouse Testican-2 Expression, Glycosylation and Effects on Neurite Outgrowth. *J Biol*
1034 *Chem* 280(12):11274-80.

1035

1036 Schuster CM, Ultsch A, Schloss P, Cox JA, Schmitt B, Betz H (1991) Molecular cloning
1037 of an invertebrate glutamate receptor subunit expressed in *Drosophila* muscle. *Science*
1038 254(5028):112-4.

1039

1040 Sears JC, Broadie K (2018) Fraile X Mental Retardation Protein regulates activity-
1041 dependent membrane trafficking and trans-synaptic signaling mediated synaptic
1042 remodeling. *Front Mol Neurosci* 10:440.

1043

1044 Shilts J, Broadie K (2017) Secreted tissue inhibitor of matrix metalloproteinase restricts
1045 *trans*-synaptic signaling to coordinate synaptogenesis. *J Cell Sci* 130(14):2344-58.

1046

1047 Speese SD, Ashley J, Jokhi V, Nunnari J, Barria R, Li Y, Ataman B, Koon A, Chang Y-
1048 T, Li Q, Moore MJ, Budnik V (2012) Nuclear Envelope Budding Enables Large
1049 Ribonucleoprotein Particle Export during Synaptic Wnt Signaling. *Cell* 149(4):832-46.

1050

1051 Stewart RA, Ramakrishnan A-B, Cadigan KM (2019) Diffusion and function of Wnt
1052 ligands. *PLoS Genet* 15(6):e1008154.

1053

1054 Takada S, Fijumori S, Shinozuka T, Takada R, Mii Y (2017) Differences in the secretion
1055 and transport of Wnt proteins. *J Biochem* 161(1):1-7.

1056

1057 Torroja L, Packard M, Gorczyca M, White K, Budnik V (1999) The *Drosophila* β -Amyloid
1058 Precursor Protein Homolog Promotes Synapse Differentiation at the Neuromuscular
1059 Junction. *J Neurosci* 19(18):7793-803.

1060

1061 Tsuda M, Kamimura K, Nakato H, Archer M, Staatz W, Fox B, Humphrey M, Olson S,
1062 Futch T, Kaluza V, Siegfried E, Stam L, Selleck SB (1999) The cell-surface
1063 proteoglycan Dally regulates Wingless signalling in *Drosophila*. *Nature* 400:276-80.

1064

1065 Vannahme C, Schübel S, Herud M, Gösling S, Hülsmann H, Paulsson M, Hartmann U,
1066 Maurer P (1999) Molecular Cloning of Testican-2: Defining a Novel Calcium-Binding
1067 Proteoglycan Family Expressed in Brain. *J Neurochem* 73(1):12-20.

1068

1069 Wagh DA, Rasse TM, Asan E, Hofbauer A, Schwenkert I, Dürrbeck H, Buchner S,
1070 Dabauvalle M-C, Schmidt M, Qin G, Wichmann C, Kittel R, Sigrist S, Buchner E (2006)
1071 Bruchpilot, a Protein with Homology to ELKS/CAST, Is Required for Structural Integrity
1072 and Function of Synaptic Active Zones in *Drosophila*. *Neuron* 49(6):833-44.

1073

1074 Yan D, Wu Y, Feng Y, Lin S-C, Lin X (2009) The Core Protein of Glypican Dally-Like
1075 Determines Its Biphasic Activity in Wingless Morphogen Signaling. *Dev Cell* 17:470-81.

1076

1077 Yook KJ, Proulx SR, Jorgensen EM (2001) Rules of Nonallelic Noncomplementation at
1078 the Synapse in *Caenorhabditis elegans*. *Genetics* 158(1):209-20.

1079

1080 Zecca M, Basler K, Struhl G (1996) Direct and Long-Range Action of a Wingless
1081 Morphogen Gradient. Cell 87(5):833-44.

1082

1083 Zhai L, Chaturvedi D, Cumberledge S (2004) *Drosophila* Wnt-1 Undergoes a
1084 Hydrophobic Modification and Is Targeted to Lipid Rafts, a Process That Requires
1085 Porcupine. JBC 279(32):33220-7

1086

1087 **Figure Legends**

1088 **Fig. 1: Carrier of Wingless (Cow) genetic locus and mutant characterization**

1089 (A) Intron/exon structure of the *cow* gene (transcript *cow-RD*; flybase.org). Arrowheads
1090 indicate gene disruption project (gdp) inserts in two different lines (03259 and 12802).
1091 The third arrowhead indicates where the published *cow*^{5Δ} deletion begins in the 3' UTR
1092 and runs 9,119 bp downstream (Chang and Sun, 2014). Below, the expanded region
1093 outlined with the red box is labeled “fwd” and “rev” to depict the RT-PCR primer pair.
1094 (B) PCR products from the genotypes listed. Control (*dfmr1* gene) and *cow* primers from
1095 the region of the *cow*^{5Δ} deletion. (C,D) RT-PCR products from the genotypes listed
1096 using both control (*dmgalectin* gene) and *cow* primers. (E) Western blot of the indicated
1097 genotypes using an anti-Cow antibody, with the total protein stain shown below. The
1098 two arrows indicate Cow protein with and without GAG chains.

1099

1100 **Fig. 2: Cow expression in embryos, larval NMJ synaptic terminal and wing disc**

1101 (A) Confocal images of stage 16 embryos co-labeled with anti-horseradish peroxidase
1102 (HRP, red) to mark neuronal membranes and anti-Cow (green) in genetic background
1103 control (*w*¹¹¹⁸, left) and *cow* null (*cow*^{GDP}/*cow*^{GDP}, right). The ventral nerve cord (VNC) is
1104 labeled. (B) Confocal images of third instar NMJ co-labeled with anti-HRP (red) and
1105 anti-Cow (green) in control (*w*¹¹¹⁸, left) and *cow* null (*cow*^{GDP}/*cow*^{GDP}, right). From non-
1106 permeabilized labeling, Cow appears secreted from a dynamic subset of synaptic
1107 boutons (arrows) and also present in the nerve bundle (arrowhead). Cow is shown
1108 without HRP in below images. White line marks the NMJ terminal HRP domain. (C)
1109 Higher magnification images of *w*¹¹¹⁸ NMJ synaptic boutons co-labeled with anti-HRP

1110 (blue), anti-Wingless (Wg, green) and anti-Cow (red), with merged image on right. White
1111 line marks the NMJ terminal HRP domain. (D) Cow-GAL4 driving UAS-Cow::eGFP in
1112 wandering third instar wing imaginal disc (left) and NMJ co-labeled with anti-HRP (red)
1113 and anti-GFP (green, right). For the NMJ, a single confocal section (0.5 μm) shows Cow
1114 punctae (arrow) within and surrounding synaptic boutons.

1115

1116 **Fig. 3: Presynaptically secreted Cow limits NMJ synaptic bouton number**

1117 (A) Confocal images of the muscle 4 NMJ co-labeled with anti-horseradish peroxidase
1118 (HRP, green) to mark the presynaptic membrane and anti-Discs Large (DLG, red) to
1119 mark the postsynaptic domain in the genetic background control (w^{1118} , left) and the
1120 *cow* null mutant (cow^{GDP}/Df , right). Synaptic bouton number is shown in a scatter plot,
1121 with mean \pm SEM. (B) Representative confocal NMJ images of motor neuron-targeted
1122 Gal4 driver control (*vglut-Gal4/+*, left), UAS-RNAi transgene control (UAS-*cow*-RNAi/+,
1123 middle) and *cow* RNAi knockdown (*vglut>cow*-RNAi, right). Satellite boutons (asterisks)
1124 are shown in the inset. Right: synaptic bouton number is shown in a scatter plot, with
1125 mean \pm SEM. (C) Representative confocal NMJ images of muscle-targeted Gal4 driver
1126 control (24B-Gal4/+), UAS-RNAi transgene control (UAS-*cow*-RNAi/+), middle) and
1127 *cow* RNAi knockdown (24B>*cow*-RNAi, right). Synaptic bouton number is quantified to
1128 the right. P-values are shown for each statistical comparison.

1129

1130 **Fig. 4: Presynaptic Cow elevation decreases Wg and increases satellite boutons**

1131 (A) Confocal images of NMJ boutons triple-labeled with anti-HRP (blue), -Cow (green)
1132 and -Wg (red), and merged (far right) comparing transgenic controls (*vglut-Gal4/+*) to

1133 motor neuron Cow overexpression condition (*vglut>cow*). Labeling done in the absence
1134 of detergent to reveal only secreted Cow and Wg. (B) Representative muscle 4 NMJ
1135 images co-labeled for presynaptic HRP (red) and postsynaptic DLG (green) comparing
1136 controls (*vglut-Gal4/+*) to neuronal Cow overexpression (*vglut>cow*). Asterisks indicate
1137 satellite boutons. The second panel shows HRP alone with arrows indicating distinct
1138 spots of HRP accumulation and the third panel shows HRP expression heatmap. (C)
1139 Quantification of confocal fluorescence intensity for Cow (left) and Wg (right) in the two
1140 conditions. (D) Quantification of synaptic bouton number (left) and the percentage of
1141 satellite boutons (right) in transgenic controls vs. *cow* neuronal overexpression. P-
1142 values are shown for each statistical comparison.

1143

1144 **Fig. 5: Presynaptic Cow limits synaptic vesicle fusion for NMJ neurotransmission**

1145 (A) Representative motor nerve stimulation-evoked EJC traces (1.5 mM [Ca²⁺]) from the
1146 *w¹¹¹⁸* genetic background control, *cow^{GDP}* homozygous mutant and *cow^{GDP}/Df* mutant.
1147 (B) Quantification of EJC amplitudes in the three genotypes shown in a scatter plot, with
1148 mean ± SEM. (C) Representative miniature EJC (mEJC) recording traces from the
1149 same genotypes. (D) Quantification of mEJC frequency (left) and amplitude (right) from
1150 the three genotypes. (E) Representative probability maps (30 sec) of SynapGCaMP
1151 imaging of mEJC events in motor neuron-targeted Gal4 driver control (*vglut-Gal4/+*, top)
1152 and *cow* RNAi knockdown (*vglut>cow-RNAi*, bottom) indicating mEJC location (dot) and
1153 frequency (color; see scale inset). (F) Quantification of SynapGCaMP event frequency
1154 (Hz/μm²; left) and fluorescence intensity (ΔF/F₀; right) shown in scatter plots, with mean
1155 ± SEM. P-values are shown for each statistical comparison.

1156

1157 **Fig. 6: Cow limits presynaptic active zones and glutamatergic synapse number**

1158 (A) Representative muscle 4 NMJ images from a confocal laser-scanning microscope
1159 (LSM) of genetic background controls (w^{1118} , left) and cow null mutants (cow^{GDP} , right)
1160 co-labeled for presynaptic membrane marker (HRP, red) and the active zone scaffold
1161 Bruchpilot (Brp, green). Brp alone is shown in right panels and quantified Brp punctae
1162 number is shown to the right. (B) High magnification synaptic bouton images with Brp
1163 punctae identified using Imaris software (asterisks, left) and volume indicated in a
1164 heatmap (scale 0.01-3.4 μm^3 , right). Quantified Brp punctae volume shown to the right.
1165 (C) Representative NMJ images from a structured illumination microscope (SIM) of
1166 controls (w^{1118}) and cow nulls (cow^{GDP}) co-labeled for both presynaptic active zones
1167 (Brp, red) and postsynaptic glutamate receptors (GluRIIC, green). The quantified Brp
1168 punctae number is shown to the right. (D) High magnification SIM images of juxtaposed
1169 Brp punctae and GluR clusters at synapses. Arrowheads indicate Brp or GluR domains
1170 without a partner, which are observed at equal frequency in both genotypes. Quantified
1171 GluR cluster number is shown to the right. P-values are shown for each statistical
1172 comparison.

1173

1174 **Fig. 7: Membrane-tethered Wg prevents cow null defects in bouton formation**

1175 (A) Representative confocal images of muscle 4 NMJs co-labeled with presynaptic HRP
1176 marker (green) and postsynaptic DLG marker (red) in Wg control ($FRT-wg$), cow null
1177 ($FRT-wg; cow^{GDP}$), tethered Wg ($NRT-wg$), and tethered Wg in cow null background
1178 ($NRT-wg; cow^{GDP}$). (B,C) Quantification of total NMJ synaptic bouton number (B) and

1179 the percentage of satellite boutons (C) in the four genotypes shown in a scatter plot,
1180 with mean \pm SEM. P-values are shown for each statistical comparison.

1181

1182 **Fig. 8: Cow and Notum act in the same Wg pathway to limit NMJ bouton number**

1183 (A) Confocal images of the muscle 4 NMJ co-labeled with presynaptic HRP marker
1184 (green) and postsynaptic DLG marker (red) in the genetic background control (w^{1118}),
1185 *cow* null heterozygote ($cow^{GDP/+}$), *notum* null heterozygote ($notum^{KO/+}$) and *cow/notum*
1186 transheterozygote ($cow^{GDP}/notum^{KO}$). Quantified bouton number is shown to the right.
1187 (B) High magnification NMJ confocal images of anti-Wg labeling at synaptic boutons of
1188 the same indicated genotypes. The presynaptic HRP marker boundary is outlined in
1189 white. Quantified Wg fluorescence intensity is shown to the right, normalized to the
1190 background control (w^{1118}). (C) Confocal images of the muscle 4 NMJ co-labeled with
1191 presynaptic HRP marker (green) and postsynaptic DLG marker (red) in the genetic
1192 background control (w^{1118}), *cow* null (cow^{GDP}/cow^{GDP}), *notum* null ($notum^{KO}/notum^{KO}$)
1193 and *cow/notum* double null ($cow^{GDP},notum^{KO}/cow^{GDP},notum^{KO}$). Quantified bouton
1194 number is shown to the right. P-values are shown for each statistical comparison.

1195

1196

1197

1198

1199

1200

1201

1202 **Tables**

1203 **Table 1: Statistical tests used to analyze data**

1204

1205 **Multimedia**

1206 **Movie 1: SynapGCaMP imaging of spontaneous quantal events in the control NMJ**

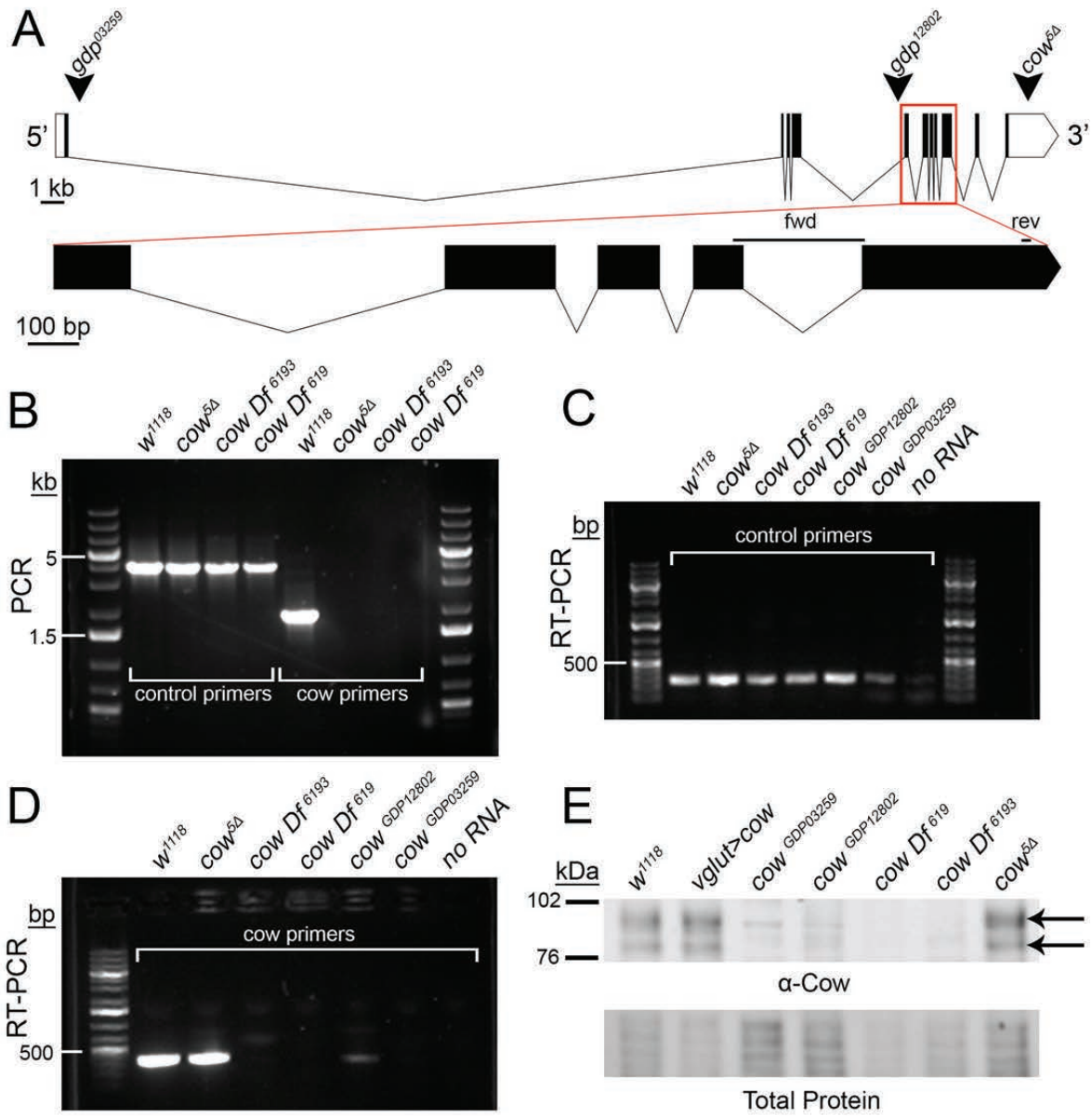
1207 Example of muscle 4 type 1b NMJ imaged in the control (*vglut-Gal4/+;*
1208 *SynapGCaMP6f/+*) with quantified data shown in Figure 4.

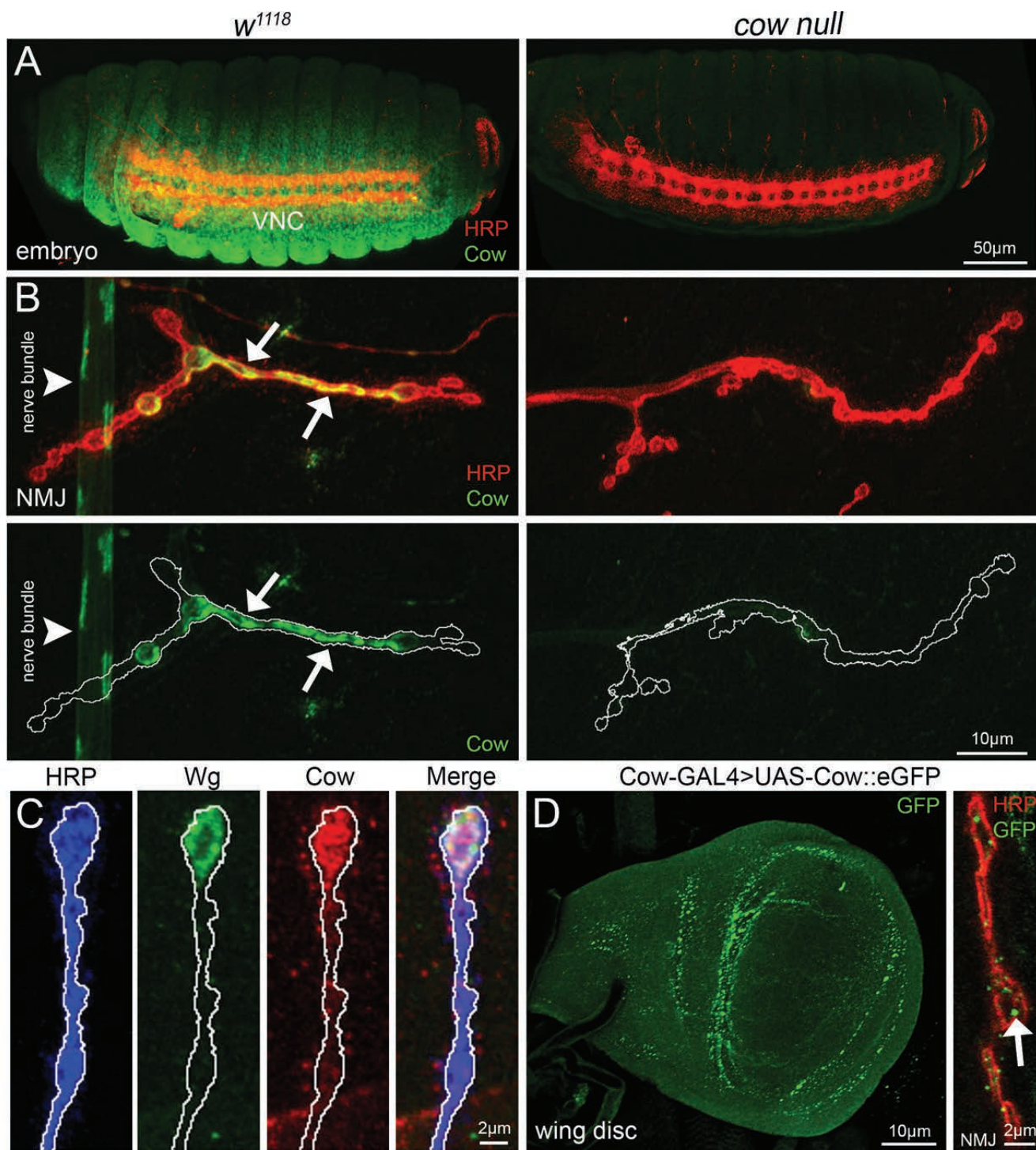
1209

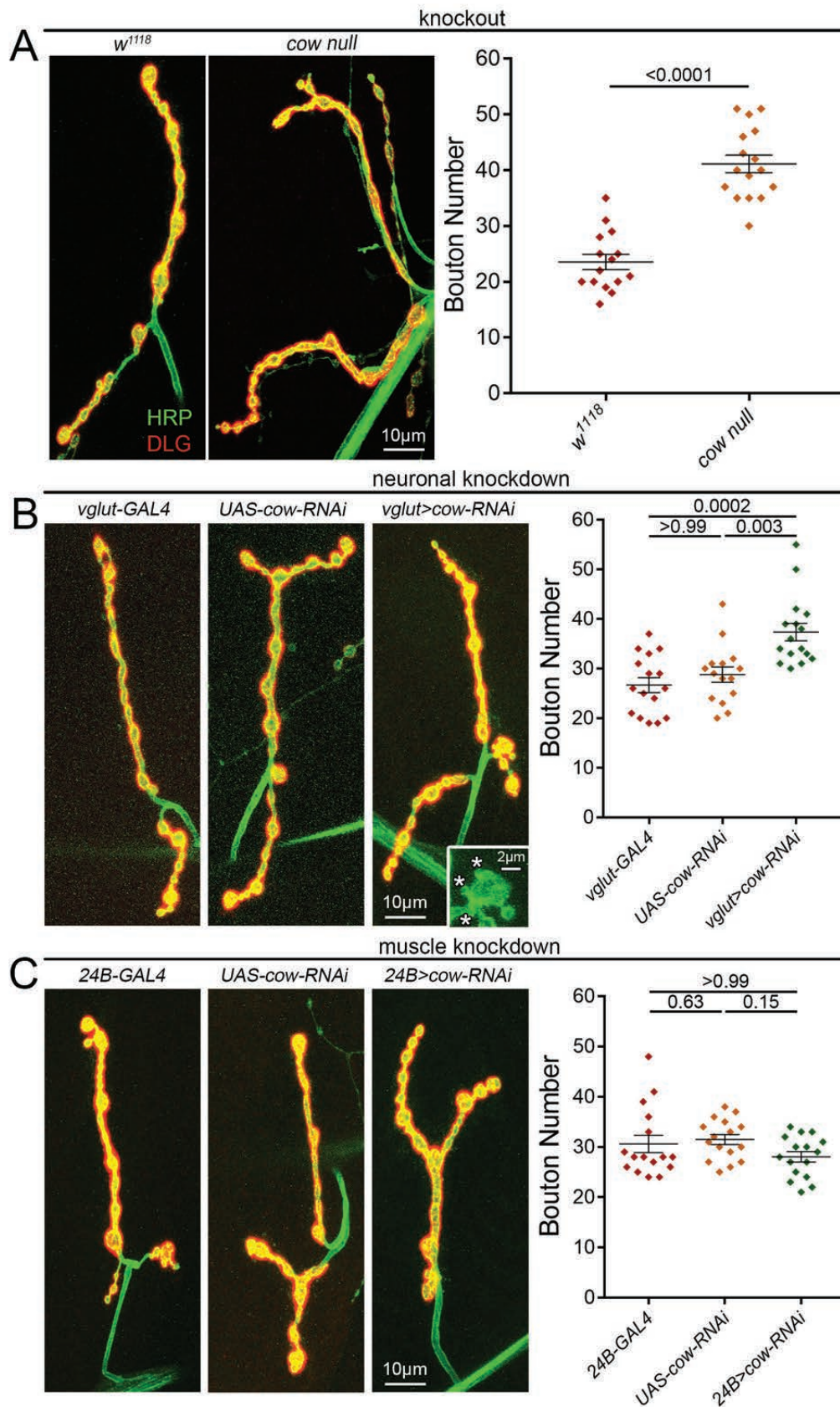
1210 **Movie 2: SynapGCaMP imaging of spontaneous quantal events in cow KD NMJ**

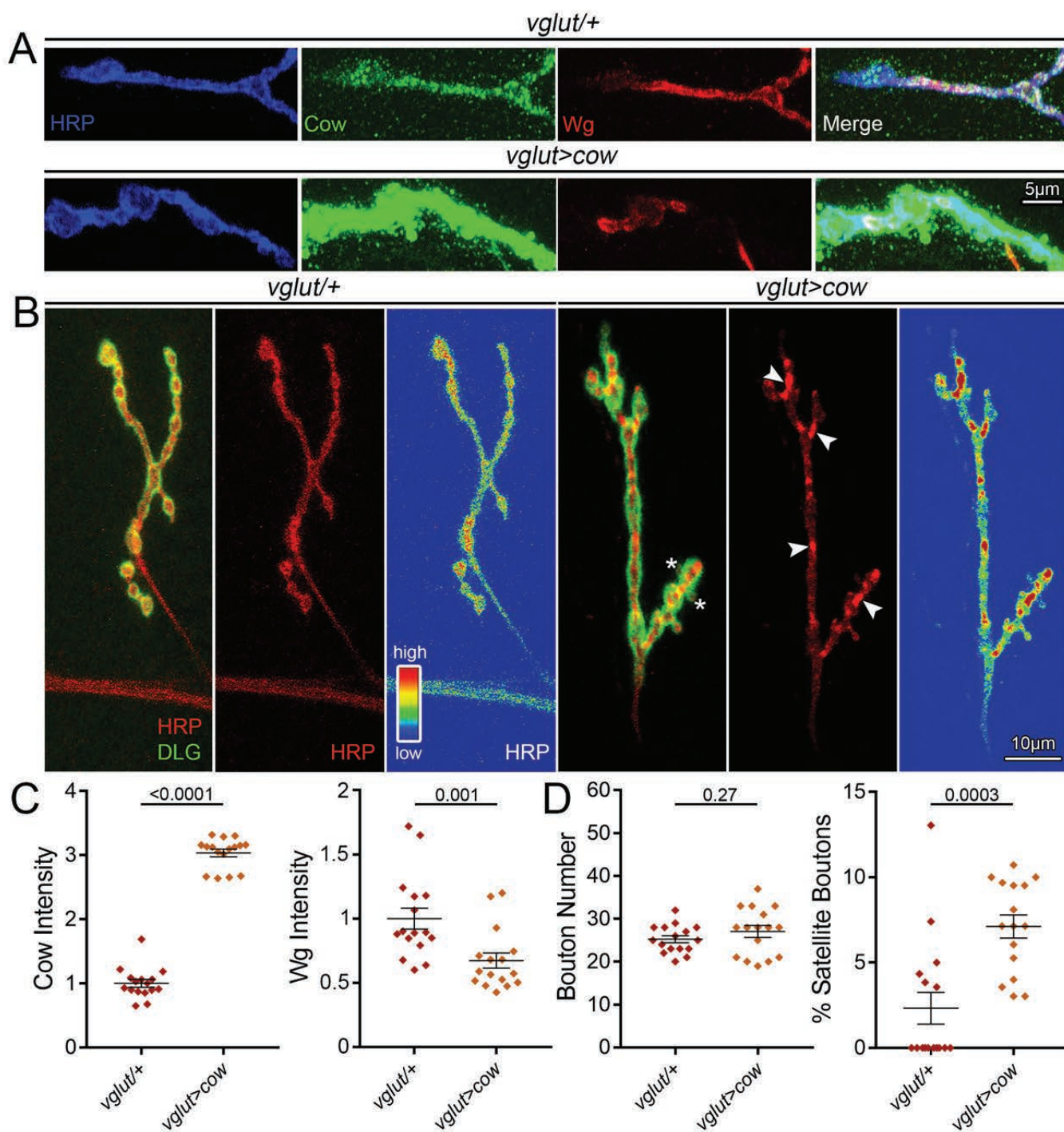
1211 Example of muscle 4 type 1b NMJ imaged following motor neuron-targeted *cow* RNAi
1212 (*vglut-Gal4>UAS-cow-RNAi;SynapGCaMP6f/+*) with quantified data shown in Figure 4.

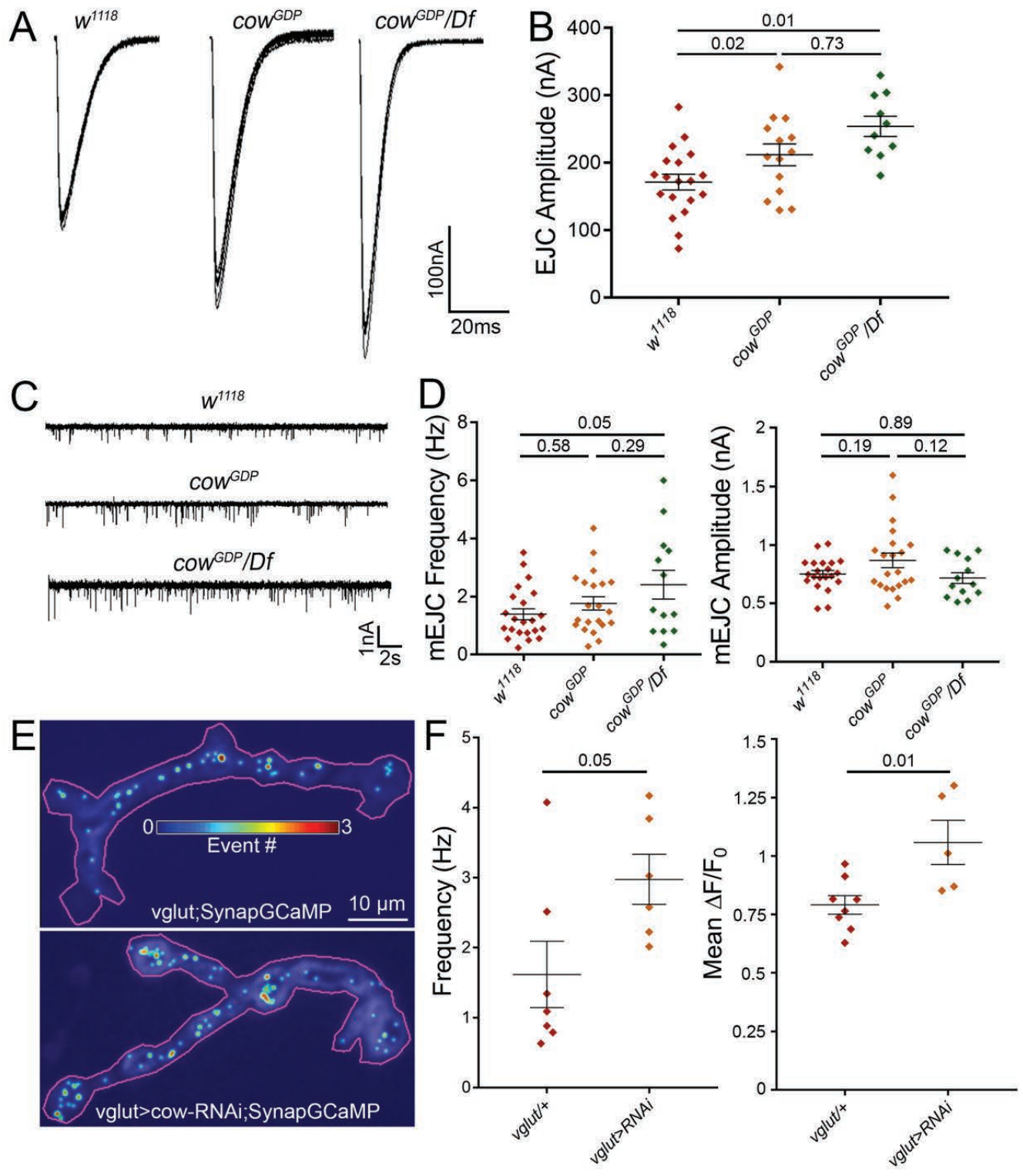
1213

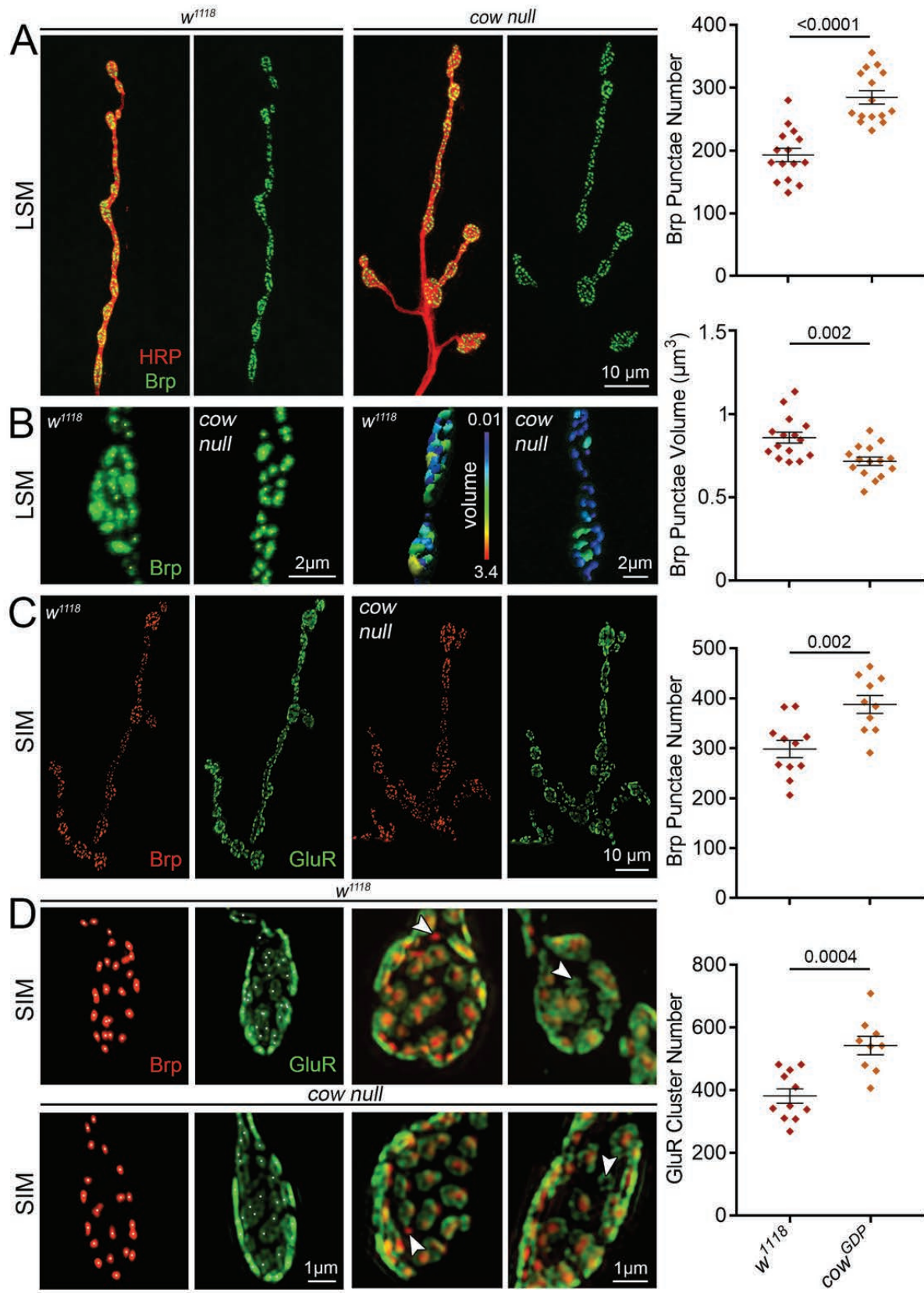


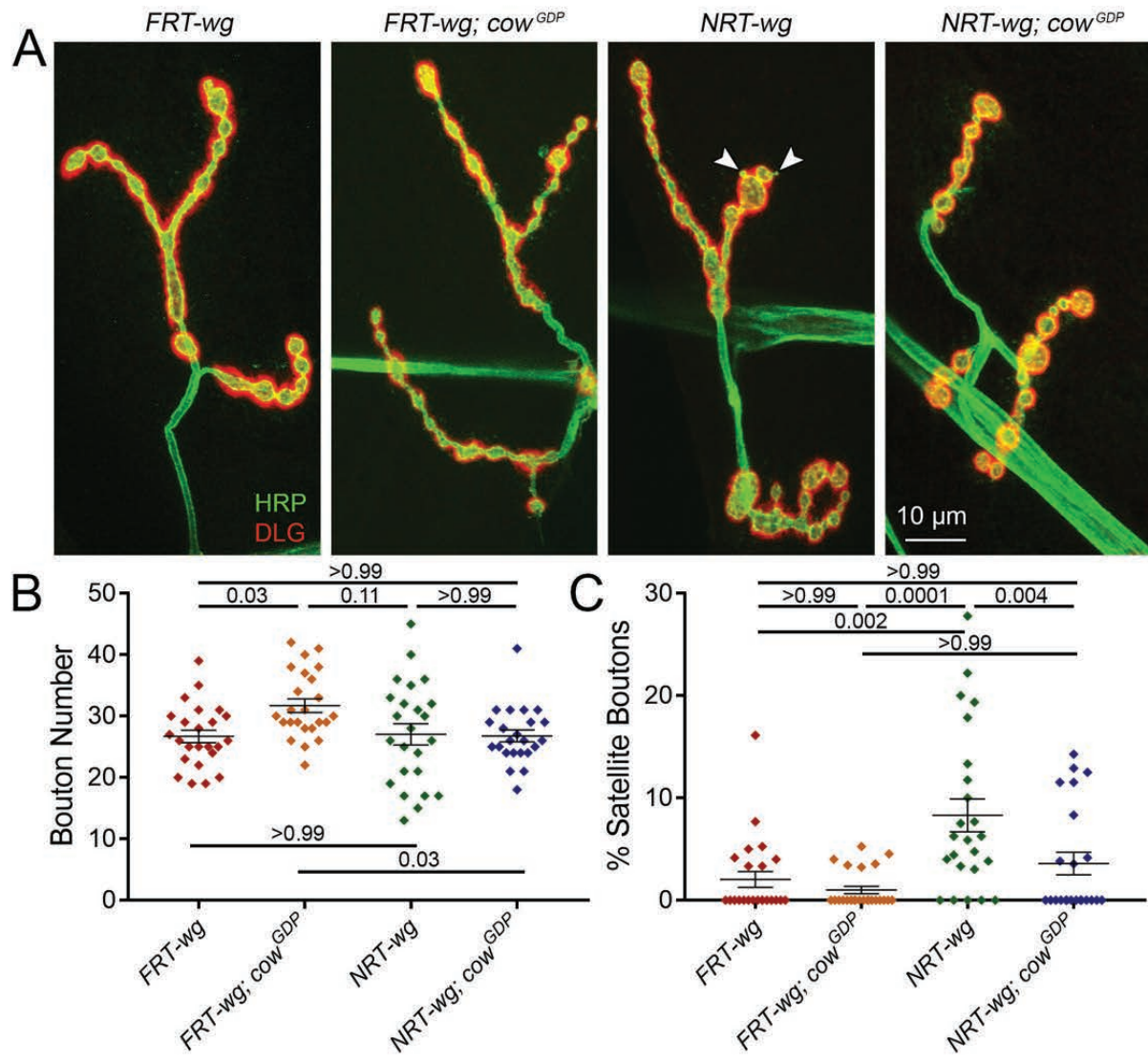


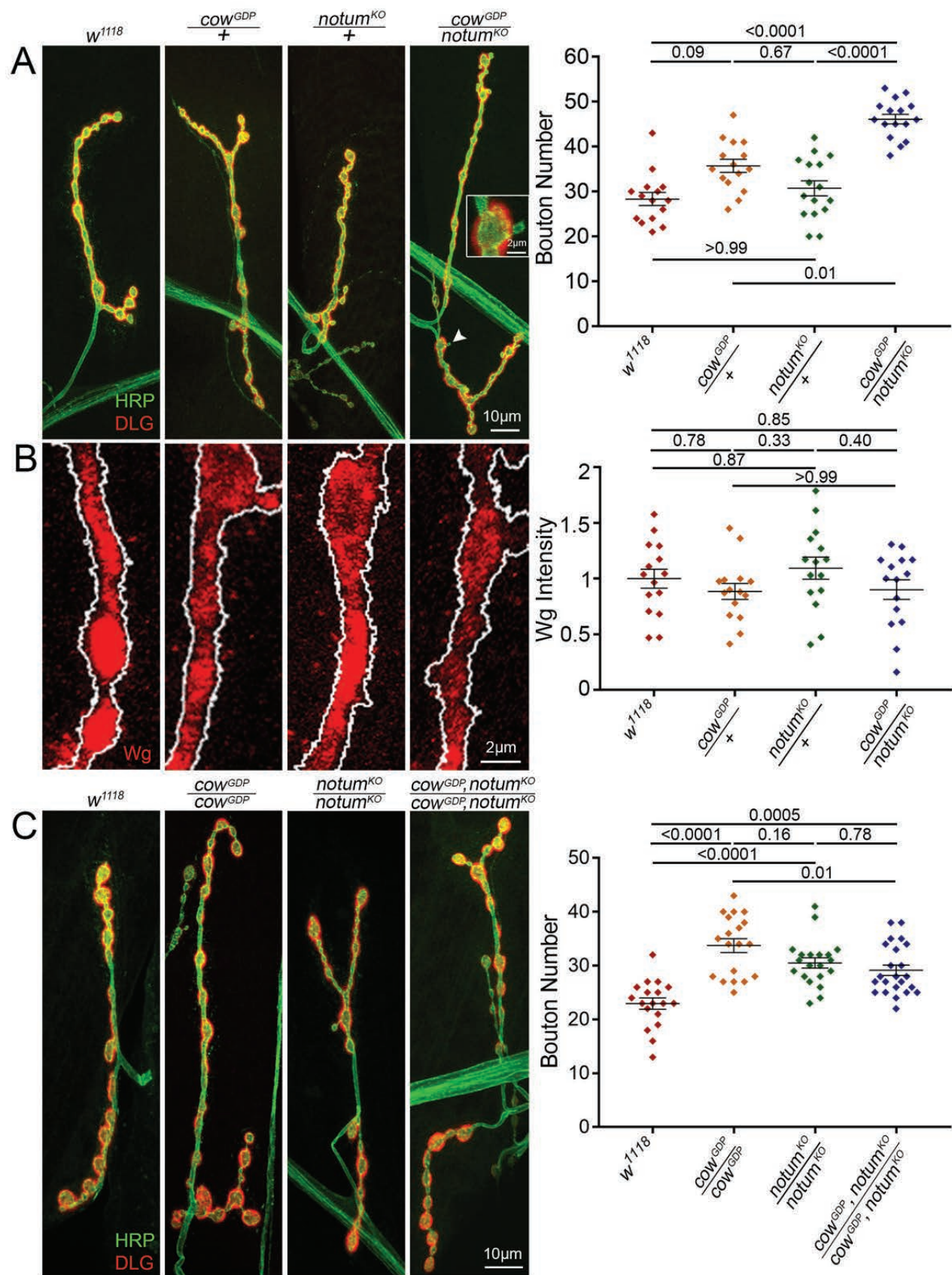


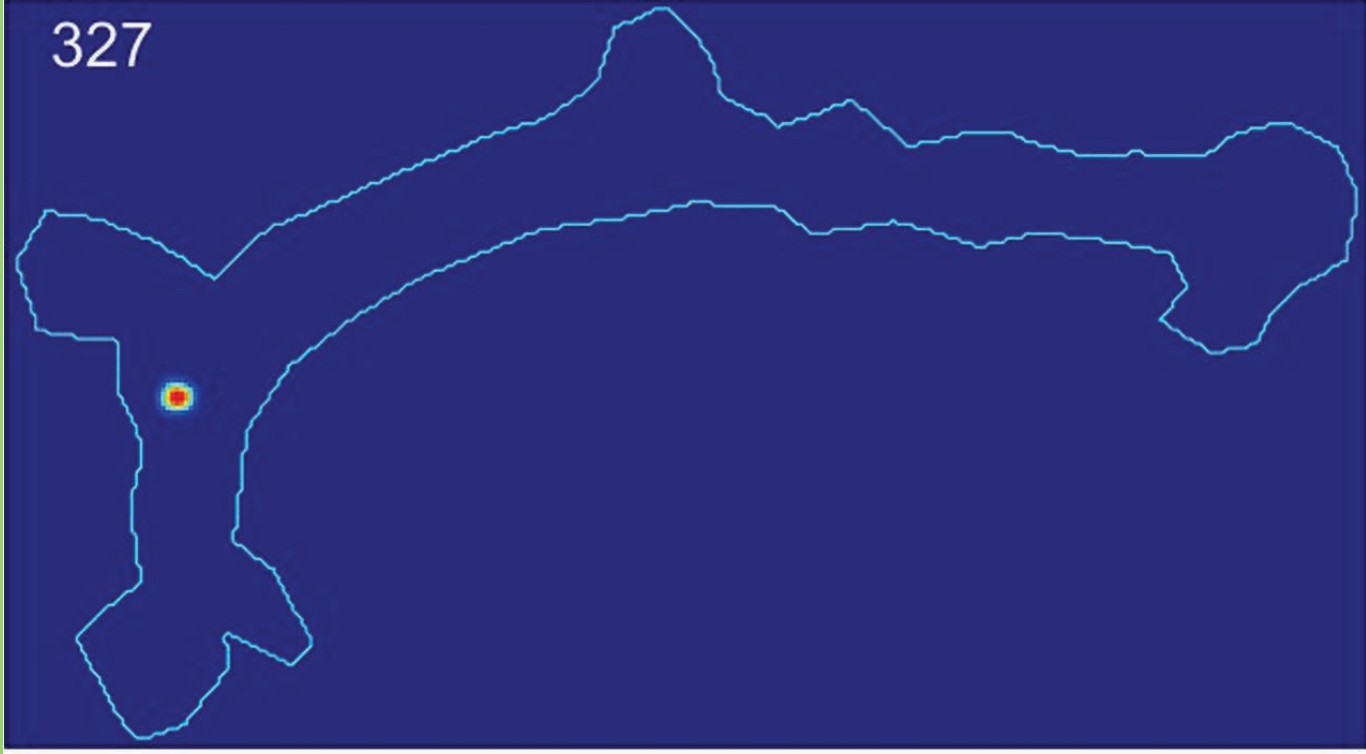




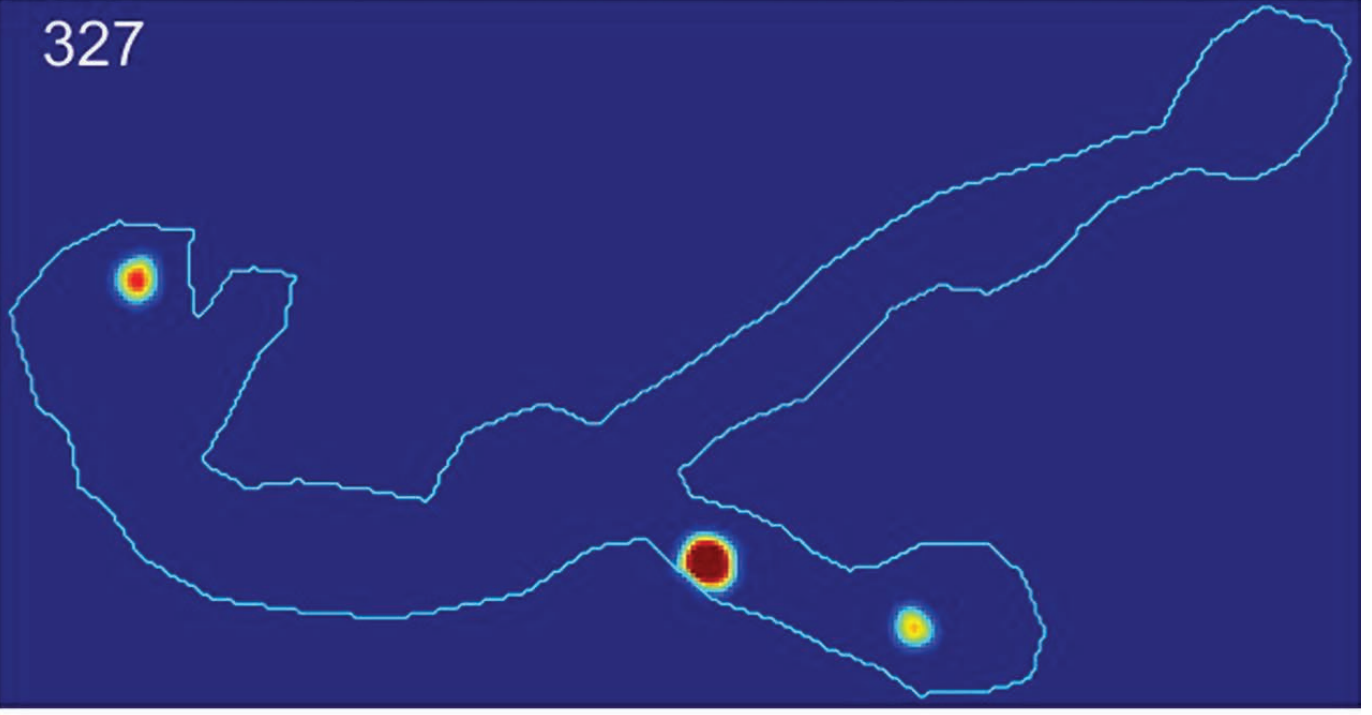








327



Feature	Comparison	Data Structure (D'Agostino normality test)	Type of Test	Sample Size (# of NMJS, # of animals)	Mean	Statistic	P-Value	Outlier Test
<u>Structure</u>								
Bouton Number	w^{1118} vs. cow^{SDP}/Df	Normal	Unpaired two-tailed t-test	w^{1118} (15,8); cow null (16,8)	23.53 vs. 41.13	$t=8.296$ $df=29$	$P<0.0001$	
Bouton Number	$vglut-GAL4$ vs. $UAS-cow-RNAi$	Not Normal	Kruskal-Wallis with Dunn's multiple comparisons test	$vglut-GAL4$ (16,8); $UAS-Cow-RNAi$ (16,8)	26.69 vs. 28.8	mean rank diff=-2.938	$P>0.9999$	
	$vglut-GAL4$ vs. $vglut>cow-RNAi$			$vglut-GAL4$ (16,8); $vglut>cow-RNAi$ (15,8)	26.69 vs. 37.38	mean rank diff=-19.09	$P=0.0002$	
	$UAS-cow-RNAi$ vs. $vglut>cow-RNAi$			$UAS-cow-RNAi$ (16,8); $vglut>cow-RNAi$ (15,8)	28.8 vs. 37.38	mean rank diff=-16.16	$P=0.0031$	
Bouton Number	$24B-GAL4$ vs. $UAS-cow-RNAi$	Not Normal	Kruskal-Wallis with Dunn's multiple comparisons test	$24B-GAL4$ (16,8); $UAS-cow-RNAi$ (16,8)	30.63 vs. 31.5	mean rank diff=-6.188	$P=0.6307$	
	$24B-GAL4$ vs. $24B>cow-RNAi$			$24B-GAL4$ (16,8); $24B>cow-RNAi$ (16,8)	30.63 vs. 28.06	mean rank diff=3.563	$P>0.9999$	
	$UAS-cow-RNAi$ vs. $24B>cow-RNAi$			$UAS-cow-RNAi$ (16,8); $24B>cow-RNAi$ (16,8)	31.5 vs. 28.06	mean rank diff=9.75	$P=0.1451$	
Bouton Number	$vglut/+$ vs. $vglut>Cow$	Normal	Unpaired two-tailed t-test	$vglut/+$ (16,8); $vglut>Cow$ (16,8)	25.25 vs. 27.06	$t=1.122$ $df=30$	$P=0.2706$	
Bouton Number	$24B/+$ vs. $24B>Cow$	Normal	Unpaired two-tailed t-test	$24B/+$ (16,8); $24B>Cow$ (16,8)	30.38 vs. 29.81	$t=0.2317$ $df=30$	$P=0.8183$	
Bouton Number	$FRT-Wg$ vs. $FRT-Wg;Cow^{SDP}$	Not Normal	Kruskal-Wallis with Dunn's multiple comparisons test	$FRT-Wg$ (24,12); $FRT-Wg;Cow^{SDP}$ (24,12)	26.71 vs. 31.71	mean rank diff=-22.29	$P=0.0300$	
	$FRT-Wg$ vs. $NRT-Wg$			$FRT-Wg$ (24,12); $NRT-Wg$ (24,12)	26.71 vs. 27.04	mean rank diff=-3.521	$P>0.9999$	
	$FRT-Wg$ vs. $NRT-Wg;Cow^{SDP}$			$FRT-Wg$ (24,12); $NRT-Wg;Cow^{SDP}$ (23,12)	26.71 vs. 26.78	mean rank diff=0.4312	$P>0.9999$	
	$FRT-Wg;Cow^{SDP}$ vs. $NRT-Wg$			$FRT-Wg;Cow^{SDP}$ (24,12); $NRT-Wg$ (24,12)	31.71 vs. 27.04	mean rank diff=18.77	$P=0.1085$	
	$FRT-Wg;Cow^{SDP}$ vs. $NRT-Wg;Cow^{SDP}$			$FRT-Wg;Cow^{SDP}$ (24,12); $NRT-Wg;Cow^{SDP}$ (23,12)	31.71 vs. 26.78	mean rank diff=22.72	$P=0.0278$	
	$NRT-Wg$ vs. $NRT-Wg;Cow^{SDP}$			$NRT-Wg$ (24,12); $NRT-Wg;Cow^{SDP}$ (23,12)	27.04 vs. 26.78	mean rank diff=3.952	$P>0.9999$	
Bouton Number	w^{1118} vs. $cow^{SDP}/+$	Not Normal	Kruskal-Wallis with Dunn's multiple comparisons test	w^{1118} (15,8); $cow^{SDP}/+$ (15,8)	28.33 vs. 35.73	mean rank diff=-15.93	$P=0.0929$	
	w^{1118} vs. $Notum^{KO}/+$			w^{1118} (15,8); $Notum^{KO}/+$ (16,8)	28.33 vs. 30.75	mean rank diff=-5.565	$P>0.9999$	
	w^{1118} vs. $cow^{SDP}/Notum^{KO}$			w^{1118} (15,8); $cow^{SDP}/Notum^{KO}$ (16,8)	28.33 vs. 46.13	mean rank diff=-35.81	$P<0.0001$	
	$cow^{SDP}/+$ vs. $Notum^{KO}/+$			$cow^{SDP}/+$ (15,8); $Notum^{KO}/+$ (16,8)	35.73 vs. 30.75	mean rank diff=10.37	$P=0.6569$	

	$cow^{GDP}/+$ vs. $cow^{GDP}/Notum^{KO}$			$cow^{GDP}/+$ (15,8); $cow^{GDP}/Notum^{KO}$ (16,8)	35.75 vs. 46.13	mean rank diff=-19.88	P=0.0129	
	$Notum^{KO}/+$ vs. $cow^{GDP}/Notum^{KO}$			$Notum^{KO}/+$ (16,8); $cow^{GDP}/Notum^{KO}$ (16,8)	30.75 vs. 46.13	mean rank diff=-30.25	P<0.0001	
Bouton Number	w^{1118} vs. cow^{GDP}/cow^{GDP}	Normal	Ordinary one-way ANOVA with Tukey's multiple comparisons test	w^{1118} (18,10); cow^{GDP}/cow^{GDP} (19,10)	22.94 vs. 33.74	q=9.731 df=76	P<0.0001	
	w^{1118} vs. $Notum^{KO}/Notum^{KO}$			w^{1118} (18,10); $Notum^{KO}/Notum^{KO}$ (20,10)	22.94 vs. 30.5	q=6.897 df=76	P<0.0001	
	w^{1118} vs. $cow^{GDP}, Notum^{KO}/cow^{GDP}, Notum^{KO}$			w^{1118} (18,10); $cow^{GDP}, Notum^{KO}/cow^{GDP}, Notum^{KO}$ (23,12)	22.94 vs. 29.13	q=5.83 df=76	P=0.0005	
	cow^{GDP}/cow^{GDP} vs. $Notum^{KO}/Notum^{KO}$			cow^{GDP}/cow^{GDP} (19,10); $Notum^{KO}/Notum^{KO}$ (20,10)	33.74 vs. 30.5	q=2.996 df=76	P=0.1564	
	cow^{GDP}/cow^{GDP} vs. $cow^{GDP}, Notum^{KO}/cow^{GDP}, Notum^{KO}$			cow^{GDP}/cow^{GDP} (19,10); $cow^{GDP}, Notum^{KO}/cow^{GDP}, Notum^{KO}$ (23,12)	33.74 vs. 29.13	q=4.407 df=76	P=0.0135	
	$Notum^{KO}/Notum^{KO}$ vs. $cow^{GDP}, Notum^{KO}/cow^{GDP}, Notum^{KO}$			$Notum^{KO}/Notum^{KO}$ (20,10); $cow^{GDP}, Notum^{KO}/cow^{GDP}, Notum^{KO}$ (23,12)	30.5 vs. 29.13	q=1.328 df=76	P=0.7838	
% Satellite Boutons	w^{1118} vs. cow^{GDP}/Df	Normal	Unpaired two-tailed t-test	w^{1118} (15,8); cow null (15,8)	3.301 vs. 3.336%	t=0.03021 df=28	P=0.9761	ROUT, Q=1%, removed 1 cow^{GDP}/Df value
% Satellite Boutons	$vglut-GAL4/+$ vs. $UAS-Cow-RNAi/+$	Normal	Ordinary one-way ANOVA with Tukey's multiple comparisons test	$vglut-GAL4/+$ (16,8); $UAS-Cow-RNAi/+$ (15,8)	2.895 vs. 2.908%	q=0.016 df=42	P>0.9999	ROUT, Q=1%, removed 2 $vglut>Cow-RNAi$ values
	$vglut-GAL4/+$ vs. $vglut>Cow-RNAi$			$vglut-GAL4/+$ (16,8); $vglut>Cow-RNAi$ (14,8)	2.895 vs. 5.772%	q=3.309 df=42	P=0.0612	
	$UAS-Cow-RNAi/+$ vs. $vglut>Cow-RNAi$			$UAS-Cow-RNAi/+$ (15,8); $vglut>Cow-RNAi$ (14,8)	2.908 vs. 5.772%	q=3.244 df=42	P=0.0677	
% Satellite Boutons	$24B-GAL4/+$ vs. $UAS-Cow-RNAi/+$	Not Normal	Kruskal-Wallis with Dunn's multiple comparisons test	$24B-GAL4/+$ (16,8); $UAS-Cow-RNAi/+$ (16,8)	0.88 vs. 2.381%	mean rank diff=-8.656	P=0.1328	
	$24B-GAL4/+$ vs. $24B>cow-RNAi$			$24B-GAL4/+$ (16,8); $24B>cow-RNAi$ (16,8)	0.88 vs. 2.806%	mean rank diff=-8.969	P=0.1114	
	$UAS-Cow-RNAi/+$ vs. $24B>cow-RNAi$			$UAS-Cow-RNAi/+$ (16,8); $24B>cow-RNAi$ (16,8)	2.381 vs. 2.806%	mean rank diff=-0.3125	P>0.9999	
% Satellite Boutons	$vglut/+$ vs. $vglut>Cow$	Not Normal	Mann-Whitney test	$vglut/+$ (16,8); $vglut>Cow$ (16,8)	2.326 vs. 7.121%	U=38	P=0.0003	
% Satellite Boutons	$24B/+$ vs. $24B>Cow$	Normal	Unpaired two-tailed t-test	$24B/+$ (16,8); $24B>Cow$ (16,8)	3.164 vs. 5.476%	t=1.177 df=30	P=0.2486	
% Satellite Boutons	$FRT-Wg$ vs. $FRT-Wg; Cow^{GDP}$	Not Normal	Kruskal-Wallis with Dunn's multiple comparisons test	$FRT-Wg$ (16,8); $FRT-Wg; Cow^{GDP}$ (16,8)	2.038 vs. 1.002%	mean rank diff=5.167	P>0.9999	

	FRT-Wg vs. NRT-Wg			FRT-Wg (16,8); NRT-Wg (16,8)	2.038 vs. 8.304%	mean rank diff=-26.08	P=0.0021	
	FRT-Wg vs. NRT-Wg;Cow ^{SDP}			FRT-Wg (16,8); NRT-Wg;Cow ^{SDP} (16,8)	2.038 vs. 3.595%	mean rank diff=-5.452	P>0.9999	
	FRT-Wg;Cow ^{SDP} vs. NRT-Wg			FRT-Wg;Cow ^{SDP} (16,8); NRT-Wg (16,8)	1.002 vs. 8.304%	mean rank diff=-31.25	P=0.0001	
	FRT-Wg;Cow ^{SDP} vs. NRT-Wg;Cow ^{SDP}			FRT-Wg;Cow ^{SDP} (16,8); NRT-Wg;Cow ^{SDP} (16,8)	1.002 vs. 3.595%	mean rank diff=-10.62	P>0.9999	
	NRT-Wg vs. NRT-Wg;Cow ^{SDP}			NRT-Wg (16,8); NRT-Wg;Cow ^{SDP} (16,8)	8.304 vs. 3.595%	mean rank diff=20.63	P=0.0038	
% Satellite Boutons	w ¹¹¹⁸ vs. cow ^{SDP} /+	Not Normal	Kruskal-Wallis with Dunn's multiple comparisons test	w ¹¹¹⁸ (15,8); cow ^{SDP} /+ (15,8)	1.89 vs. 3.079%	mean rank diff=-7.867	P>0.9999	
	w ¹¹¹⁸ vs. Notum ^{KO} /+			w ¹¹¹⁸ (15,8); Notum ^{KO} /+ (16,8)	1.89 vs. 3.379%	mean rank diff=-10.95	P=0.4586	
	w ¹¹¹⁸ vs. cow ^{SDP} /Notum ^{KO}			w ¹¹¹⁸ (15,8); cow ^{SDP} /Notum ^{KO} (16,8)	1.89 vs. 3.337%	mean rank diff=-13.2	P=0.1961	
	cow ^{SDP} /+ vs. Notum ^{KO} /+			cow ^{SDP} /+ (15,8); Notum ^{KO} /+ (16,8)	3.079 vs. 3.379%	mean rank diff=-3.079	P>0.9999	
	cow ^{SDP} /+ vs. cow ^{SDP} /Notum ^{KO}			cow ^{SDP} /+ (15,8); cow ^{SDP} /Notum ^{KO} (16,8)	3.079 vs. 3.337%	mean rank diff=-5.329	P>0.9999	
	Notum ^{KO} /+ vs. cow ^{SDP} /Notum ^{KO}			Notum ^{KO} /+ (16,8); cow ^{SDP} /Notum ^{KO} (16,8)	3.379 vs. 3.337%	mean rank diff=-2.25	P>0.9999	
% Satellite Boutons	w ¹¹¹⁸ vs. cow ^{SDP} /cow ^{SDP}	Not Normal	Kruskal-Wallis with Dunn's multiple comparisons test	w ¹¹¹⁸ (18,10); cow ^{SDP} /cow ^{SDP} (19,10)	1.904 vs. 1.623%	mean rank diff=2.006	P>0.9999	
	w ¹¹¹⁸ vs. Notum ^{KO} /Notum ^{KO}			w ¹¹¹⁸ (18,10); Notum ^{KO} /Notum ^{KO} (20,10)	1.904 vs. 2.443%	mean rank diff=-1.989	P>0.9999	
	w ¹¹¹⁸ vs. cow ^{SDP} ,Notum ^{KO} /cow ^{SDP} ,Notum ^{KO}			w ¹¹¹⁸ (18,10); cow ^{SDP} ,Notum ^{KO} /cow ^{SDP} ,Notum ^{KO} (23,12)	1.904 vs. 0.5223%	mean rank diff=9.155	P=0.7029	
	cow ^{SDP} /cow ^{SDP} vs. Notum ^{KO} /Notum ^{KO}			cow ^{SDP} /cow ^{SDP} (19,10); Notum ^{KO} /Notum ^{KO} (20,10)	1.623 vs. 2.443%	mean rank diff=-3.995	P>0.9999	
	cow ^{SDP} /cow ^{SDP} vs. cow ^{SDP} ,Notum ^{KO} /cow ^{SDP} ,Notum ^{KO}			cow ^{SDP} /cow ^{SDP} (19,10); cow ^{SDP} ,Notum ^{KO} /cow ^{SDP} ,Notum ^{KO} (23,12)	1.623 vs. 0.5223%	mean rank diff=7.149	P>0.9999	
	Notum ^{KO} /Notum ^{KO} vs. cow ^{SDP} ,Notum ^{KO} /cow ^{SDP} ,Notum ^{KO}			Notum ^{KO} /Notum ^{KO} (20,10); cow ^{SDP} ,Notum ^{KO} /cow ^{SDP} ,Notum ^{KO} (23,12)	2.443 vs. 0.5223%	mean rank diff=-11.14	P=0.2978	
Expression								
Cow Intensity	vglut/+ vs. vglut>Cow	Not Normal	Mann-Whitney test	vglut/+ (16,8); vglut>Cow (16,8)	1 vs. 3.035	U=0	P<0.0001	
Cow Intensity	24B/+ vs. 24B>Cow	Not Normal	Mann-Whitney test	24B/+ (16,8); 24B>Cow (16,8)	1 vs. 3.907	U=0	P<0.0001	
Wg Intensity	vglut/+ vs. vglut>Cow	Not Normal	Mann-Whitney test	vglut/+ (16,8); vglut>Cow (16,8)	1 vs. 0.6731	U=46	P=0.0014	
Wg Intensity	24B/+ vs. 24B>Cow	Normal	Unpaired two-tailed t-test	24B/+ (16,8); 24B>Cow (16,8)	1 vs. 1.518	t=3.266 df=30	P=0.0027	

Wg Intensity	w^{1118} vs. $cow^{GDP}/+$	Normal	Ordinary one-way ANOVA with Tukey's multiple comparisons test	w^{1118} (15,8); $cow^{GDP}/+$ (15,8)	1 vs. 0.885	q=1.328 df=56	P=0.7840		
	w^{1118} vs. $Notum^{KO}/+$			w^{1118} (15,8); $Notum^{KO}/+$ (15,8)	1 vs. 1.095	q=1.094 df=56	P=0.8660		
	w^{1118} vs. $cow^{GDP}/Notum^{KO}$			w^{1118} (15,8); $cow^{GDP}/Notum^{KO}$ (15,8)	1 vs. 0.9014	q=1.139 df=56	P=0.8515		
	$cow^{GDP}/+$ vs. $Notum^{KO}/+$			$cow^{GDP}/+$ (15,8); $Notum^{KO}/+$ (15,8)	0.885 vs. 1.095	q=2.422 df=56	P=0.3268		
	$cow^{GDP}/+$ vs. $cow^{GDP}/Notum^{KO}$			$cow^{GDP}/+$ (15,8); $cow^{GDP}/Notum^{KO}$ (15,8)	0.885 vs. 0.9014	q=0.1886 df=56	P=0.9991		
	$Notum^{KO}/+$ vs. $cow^{GDP}/Notum^{KO}$			$Notum^{KO}/+$ (15,8); $cow^{GDP}/Notum^{KO}$ (15,8)	1.095 vs. 0.9014	q=2.234 df=56	P=0.3985		
Brp Punctae Number	w^{1118} vs. cow^{GDP}	Normal	Unpaired two-tailed t-test	w^{1118} (15,8); cow^{GDP} (15,8)	193.1 vs. 284.8	t=6.152 df=28	P<0.0001		
Brp Punctae Volume	w^{1118} vs. cow^{GDP}	Normal	Unpaired two-tailed t-test	w^{1118} (15,8); cow^{GDP} (15,8)	0.8576 vs. 0.7164 μm^3	t=3.429 df=28	P=0.0019	ROUT, Q=1%, removed 1 cow^{GDP} value	
Brp Punctae Number	w^{1118} vs. cow^{GDP}	Normal	Unpaired two-tailed t-test	w^{1118} (11,8); cow^{GDP} (10,8)	298.6 vs. 387.9	t=3.598 df=19	P=0.0019		
GluR Cluster Number	w^{1118} vs. cow^{GDP}	Normal	Unpaired two-tailed t-test	w^{1118} (11,8); cow^{GDP} (9,6)	382 vs. 542.8	t=4.353 df=18	P=0.0004		
Function									
EJC Amplitude	w^{1118} vs. cow^{GDP}	Normal	Ordinary one-way ANOVA with Tukey's multiple comparisons test	w^{1118} (26,20); cow^{GDP} (20,18)	171.6 vs. 212.1 nA	q=3.868 df=53	P=0.0227	ROUT, Q=1%, removed 1 cow^{GDP} value	
	w^{1118} vs. cow^{GDP}/Df			w^{1118} (26,20); cow^{GDP}/Df (10,9)	171.6 vs. 254.2 nA	q=4.197 df=53	P=0.0123		
	cow^{GDP} vs. cow^{GDP}/Df			cow^{GDP} (20,18); cow^{GDP}/Df (10,9)	212.1 vs. 254.2 nA	q=1.063 df=53	P=0.7341		
EJC Amplitude	w^{1118} vs. $cow^{GDP}/+$	Normal	Ordinary one-way ANOVA with Tukey's multiple comparisons test	w^{1118} (10,6); $cow^{GDP}/+$ (11,6)	217.2 vs. 234.9 nA	q=0.9383 df=40	P=0.9101		
	w^{1118} vs. $notum^{KO}/+$			w^{1118} (10,6); $notum^{KO}/+$ (11,9)	217.2 vs. 214.1 nA	q=0.1649 df=40	P=0.9994		
	w^{1118} vs. $cow^{GDP}/notum^{KO}$			w^{1118} (10,6); $cow^{GDP}/notum^{KO}$ (12,7)	217.2 vs. 235.9 nA	q=1.009 df=40	P=0.8911		
	$cow^{GDP}/+$ vs. $notum^{KO}/+$			$cow^{GDP}/+$ (11,6); $notum^{KO}/+$ (11,9)	234.9 vs. 214.1 nA	q=1.13 df=40	P=0.8543		
	$cow^{GDP}/+$ vs. $cow^{GDP}/notum^{KO}$			$cow^{GDP}/+$ (11,6); $cow^{GDP}/notum^{KO}$ (12,7)	234.9 vs. 235.9 nA	q=0.05304 df=40	P>0.9999		
	$notum^{KO}/+$ vs. $cow^{GDP}/notum^{KO}$			$notum^{KO}/+$ (11,9); $cow^{GDP}/notum^{KO}$ (12,7)	214.1 vs. 235.9 nA	q=1.208 df=40	P=0.8282		

mEJC Frequency	w^{1118} vs. cow^{GDF}	Normal	Ordinary one-way ANOVA with Tukey's multiple comparisons test	w^{1118} (22,17); cow^{GDF} (21,15)	1.396 vs. 1.765 Hz	$q=1.419$ $df=53$	$P=0.5780$	
	w^{1118} vs. cow^{GDF}/Df			w^{1118} (22,17); cow^{GDF}/Df (13,11)	1.396 vs. 2.41 Hz	$q=3.406$ $q=53$	$P=0.0503$	
	cow^{GDF} vs. cow^{GDF}/Df			cow^{GDF} (21,15); cow^{GDF}/Df (13,11)	1.764 vs. 2.41 Hz	$q=2.15$ $df=53$	$P=0.2897$	
mEJC Frequency	$vglut-GAL4/+$ vs. $vglut>Cow-RNAi$	Normal	Unpaired two-tailed t-test	$vglut-GAL4/+$ (10,7); $vglut>Cow-RNAi$ (11,7)	1.497 vs. 2.449 Hz	$t=2.142$ $df=19$	$P=0.0454$	ROUT, $Q=1\%$, removed 1 $vglut-GAL4/+$ value
mEJC Amplitude	w^{1118} vs. cow^{GDF}	Normal	Ordinary one-way ANOVA with Tukey's multiple comparisons test	w^{1118} (21,16); cow^{GDF} (21,15)	0.7518 vs. 0.8682 nA	$q=2.506$ $df=52$	$P=0.1889$	ROUT, $Q=1\%$, removed 1 w^{1118} value
	w^{1118} vs. cow^{GDF}/Df			w^{1118} (21,16); cow^{GDF}/Df (13,11)	0.7518 vs. 0.7165 nA	$q=0.6647$ $df=52$	$P=0.8856$	
	cow^{GDF} vs. cow^{GDF}/Df			cow^{GDF} (21,15); cow^{GDF}/Df (13,11)	0.8682 vs. 0.7165 nA	$q=2.857$ $df=52$	$P=0.1175$	
mEJC Amplitude	$vglut-GAL4/+$ vs. $vglut>Cow-RNAi$	Normal	Unpaired two-tailed t-test	$vglut-GAL4/+$ (11,7); $vglut>Cow-RNAi$ (11,7)	0.8015 vs. 0.8446 nA	$t=0.8011$ $df=20$	$P=0.4325$	
Frequency	$vglut/+$ vs. $vglut>RNAi$	Not Normal (Shapiro-Wilk normality test performed because N too small)	Mann-Whitney test	$vglut/+$ (7,4); $vglut>RNAi$ (6,3)	1.617 vs. 2.977 Hz/ μm^2	$U=7$	$P=0.0513$	
Mean $\Delta F/F_0$	$vglut/+$ vs. $vglut>RNAi$	Normal (Shapiro-Wilk normality test performed because N too small)	Unpaired two-tailed t-test	$vglut/+$ (8,4); $vglut>RNAi$ (5,3)	0.7912 vs. 1.058 $\Delta F/F_0$	$t=3.013$ $df=11$	$P=0.0118$	